High-spin structure in ^{181,183}Au

W. F. Mueller,* H. Q. Jin,† J. M. Lewis, W. Reviol, and L. L. Riedinger
Department of Physics and Astronomy, University of Tennessee, Knoxville, Tennessee 37996-1200

M. P. Carpenter
Physics Division, Argonne National Laboratory, Argonne, Illinois 60439

C. Baktash, J. D. Garrett, N. R. Johnson, I. Y. Lee,‡ F. K. McGowan, and C. -H. Yu
Physics Division, Oak Ridge National Laboratory, Oak Ridge, Tennessee 37831

S. Cwiok
Institute of Physics, Warsaw University of Technology, ul. Koszykowa 75, PL-00-662 Warsaw, Poland
(Received 19 October 1998)

High-spin states were studied in ^{181,183}Au and resulted in the identification of several new prolate rotational bands based on $\pi i_{13/2}$, $\pi h_{9/2}$, $\pi f_{7/2}$, and $\pi h_{11/2}$ configurations. The alignment and moment of inertia features of the intruder bands are compared with ground-state bands in Pt nuclei. From these features, it can be concluded that a strongly interacting $(\pi h_{9/2})^2$ alignment is occurring in the $\pi i_{13/2}$ bands in Au and the ground-state bands in Pt. In addition, bandhead energies and deformation parameters are calculated for deformed configurations in the framework of a microscopic-macroscopic shell-correction model. These calculations are compared with experimental values in Re and Ir, as well as, Au isotopes. Interaction properties between known $\pi h_{9/2}$ and $\pi f_{7/2}$ rotational bands are also discussed and compared with results from a cranked-shell model. Experimental $B(M1)/B(E2)$ ratios between these bands are compared with results from a particle-rotor calculation. [S0556-2813(99)05304-2]

PACS number(s): 27.70.+q, 21.10.−k, 23.20.Lv, 21.60.Ev

I. INTRODUCTION

Gold nuclei ($Z=79$) represent an excellent laboratory to study the various shapes that can occur so near to a closed shell ($Z=82$). While slightly oblate shapes dominate the low-energy structure of heavier Au nuclei ($A>187$) [1], prolate shapes are lower in energy for the lighter isotopes. The stability of this prolate minimum is dependent on the proton single-particle states of the highest angular momentum, $i_{13/2}$ and $h_{9/2}$. The $\pi h_{9/2}$ rotational band lies lowest in energy for odd-A Au nuclei, but the prolate-driving intruder orbital $\frac{1}{2}[660](\pi i_{13/2})$ comes lower in energy for the lighter Au nuclei. We have performed earlier measurements on ^{185}Au$_{106}$ [2] and ^{187}Au$_{108}$ [3], and observed a strongly prolate $i_{13/2}$ band based at 860 and 1122 keV, respectively. This paper describes our more recent measurements on ^{181,183}Au, which now span the neutron midshell point ($N=104$) and allow us to study the behavior of these various deformed bands in isotopes where the deformation should start to decrease (beyond midshell). It is important to understand the properties of the proton intruder bands as one progresses toward the proton drip line ($N=92$).

In addition to the first measurement of rotational bands in ^{181,183}Au, theoretical calculations to understand the observed properties are also presented in this article. The experimental setups and details of the data reduction are described in Secs. II and III. Level schemes and justification for these schemes are presented in Secs. IV A and IV B for ^{183}Au and ^{181}Au, respectively. Because of their similar nature, the configuration assignments for the rotational bands in these two nuclei are discussed together in Sec. V. A comparison of these data, as well as experimental values from other neighboring nuclei, is presented in Sec. VI. This section is divided into two parts. The first (Sec. VI A) compares the results of bandhead energy and deformation calculations from a microscopic-macroscopic shell-correction model with experimentally known bandheads of prolate structures in Re, Ir, and Au. The second part (Sec. VI B) discusses the rather unique features of the interaction between $\pi h_{9/2}$ and $\pi f_{7/2}$ configurations. As part of this discussion, experimental $B(M1)/B(E2)$ ratios are compared with values from particle-rotor calculations. Concluding remarks are presented in Sec. VII.

II. EXPERIMENTAL SETUP

The object of this study was to observe the high-spin states in ^{183}Au and ^{181}Au from their discrete γ decay. Experiments for each nucleus were performed at the Holifield Heavy Ion Research Facility at Oak Ridge National Laboratory using the Spin Spectrometer array.

The experiment to observe states in ^{183}Au utilized the ^{152}Sm(^{35}Cl,4n) heavy-ion fusion-evaporation reaction at a beam energy of 170 MeV. The beam was focused on two ^{152}Sm target foils of 98% enrichment and 0.5 mg/cm^2 thick-

*Present address: Instituut voor Kern- en Stralingfysica, Katholieke Universiteit Leuven, B-3001 Leuven, Belgium.

†Present address: NASA Ames Research Laboratory, M/S T27A-1, Moffett Field, CA 94035-1000.

‡Present address: Nuclear Science Division, Lawrence Berkeley National Laboratory, Berkeley, CA 94720.

ness arranged in a stack. For this experiment 11 of the NaI(Tl) elements (leaving 61) from the Spin Spectrometer were removed and replaced with an equivalent number of ~25%-relative-efficiency high-purity Ge detectors, nine of which had Compton-suppression units. The angle positions (and number at that angle) of these counters were 24.7°(3), 63.4°(3), 92.7°(1), 116.6°(2), and 155.3°(2) with respect to the beam axis. With this setup approximately 200×10^6 events were collected with a hardware condition of at least two Ge and five NaI(Tl) elements firing in prompt coincidence.

Excited states in ^{181}Au were produced in the reaction ^{150}Sm(^{35}Cl,4n) at a beam energy of 168 MeV. The setup for this experiment involved 18 Compton-suppressed ~25%-relative-efficiency Ge detectors and 52 NaI(Tl) elements of the Spin Spectrometer. For this setup, the angle positions (and number at that angle) of the Ge counters were 24.7°(3), 41.4°(2), 63.4°(4), 116.6°(4), 138.6°(2), and 155.3°(3) with respect to the beam axis. The target consisted of two self-supporting 0.5-mg/cm^2-thick foils to allow the recoiling nuclei to fully decay in flight. The ^{150}Sm target material was enriched to 95%. Ge-Ge coincidences were collected under the condition that at least six NaI elements fired in prompt coincidence. In this experiment, $\sim95\times10^6$ triggered events were recorded on tape.

III. DATA REDUCTION AND ANALYSIS

In both reactions, ^{152}Sm(^{35}Cl,$xpxn$) and ^{150}Sm(^{35}Cl,$xpxn$), the primary residue is the 4n evaporation channel (^{183}Au and ^{181}Au, respectively), with the largest competition coming from the $p3n$ channel (^{183}Pt, ^{181}Pt) and fission. For enhancement of the γ decays associated with ^{183}Au and ^{181}Au from the other reaction products, appropriate cuts were made on NaI fold (K) and total energy (H). In addition, coincidence relations between the transitions of interest and Au $K\alpha$ x rays, which could be distinguished from the ~2-keV [4] lower Pt x rays, were used to assign newly observed γ rays to the respective Au nucleus. These data were presorted off line to gain-match the Ge energy signals as well as correct for the Doppler shifts at different detector angles caused by the decay of the recoils in flight.

Because of the similar reactions for the two experiments, the chosen H and K for the two analyses are very similar. From the analysis of the γ-ray intensities in the H and K gates, the condition $10\leqslant K\leqslant30$ was found to be optimum. With this gate, most of the intensity of second largest byproduct in each reaction [^{182}Pt in the ^{152}Sm(^{35}Cl,$xnxp$) reaction and ^{180}Pt in ^{150}Sm(^{35}Cl,$xnxp$)] is removed. At the same time, a significant portion of the yield of the primary residue (^{183}Au and ^{181}Au, respectively) is still kept. With this condition the Ge energy data were sorted into a K-gated ($10\leqslant K\leqslant30$) symmetrized γ-γ matrix involving all angle positions. An angle-sorted γ-γ matrix was created with a slightly different gating requirement of $8\leqslant K\leqslant30$. For this matrix the six detectors at angles 24.7° and 155.3° (referred to as the 24° axis) were sorted against the eight detectors at 63.4° and 116.6°(63° axis). The lower-K requirement for the angle-sorted matrix was chosen to increase the intensity of the newly identified Au lines as a compensation for the fewer number of detectors.

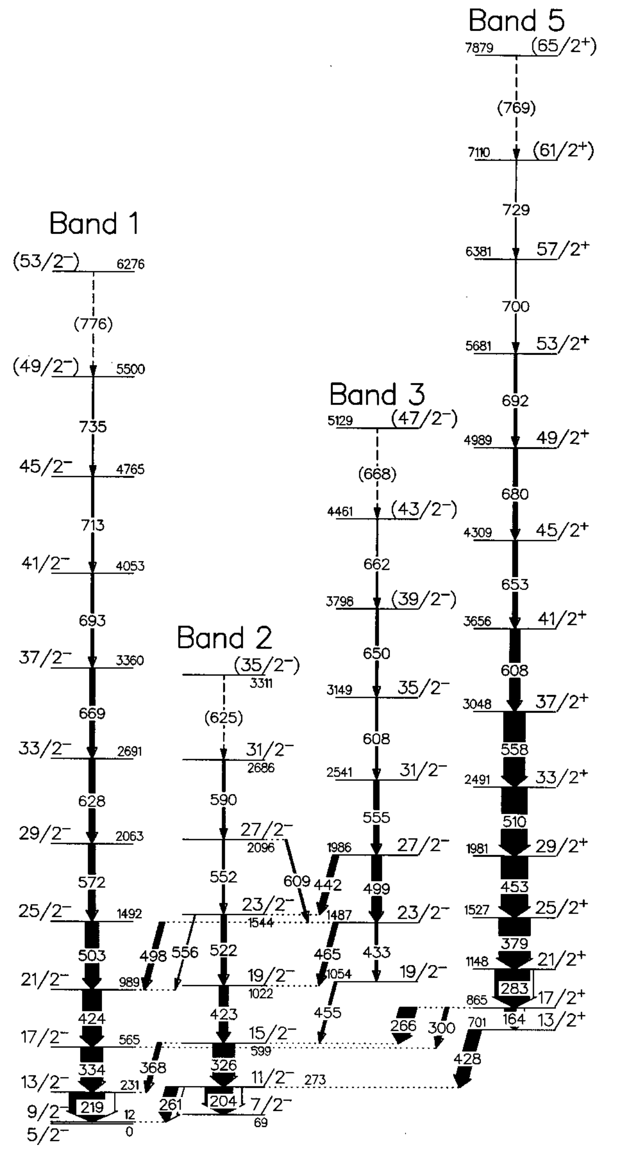

FIG. 1. Level scheme for ^{183}Au. The widths of the arrows represent the intensities of the observed transitions and the black and white shading corresponds to the γ-ray (measured) and internal-conversion (calculated) intensities, respectively. Assignments of spin and parity of levels are discussed in the text. The band labels are chosen such that they compare with similar bands in Fig. 4.

IV. RESULTS

A. ^{183}Au

Excited states in ^{183}Au up to $I^\pi=\frac{9}{2}\hbar$ have been previously studied from the β^+/[electron capture (EC)] decay of ^{183}Hg [5]. The data in the present article represent the first in-beam study performed on this nucleus. The newly established level scheme of ^{183}Au is shown in Fig. 1. Band labels are introduced to ease the discussion. The spins of the levels in Fig. 1 are based on the assumption that the lowest level observed in this work has a spin and parity of $I^\pi=\frac{9}{2}^-$. The feeding into the lower-lying $\frac{5}{2}^-$ level also shown in Fig. 1 was not observed in this experiment. However, for completeness this state is shown in the proposed level scheme, since it was established in previous experiments on ^{183}Au that are referenced below.

The assignments for the lowest spin states ($\frac{5}{2}$, $\frac{9}{2}$) are based on the systematics between levels observed in ^{183}Au and ^{185}Au. Spins and parities for the low-energy levels in ^{185}Au were established from conversion electron measurements by Kahler *et al.* [6] and in a β^+/EC experiment by Bourgeois *et al.* [7]. A spin and parity of $I^\pi = \frac{9}{2}^-$ was established for the 12-keV level in ^{183}Au by Macias-Marques *et al.* [5]. The lowest state observed in the heavy-ion fusion evaporation leading to ^{185}Au [2] was the $\frac{9}{2}^-$ level in the $\pi h_{9/2}$ band. In ^{185}Au and ^{183}Au, the $\frac{9}{2}^-$ level in these nuclei is measured to be 8.9 and 12.3 keV above the ground state, respectively.

Assignment of spins for the excited states are based on directional correlation (DCO) ratio measurements of γ decays. As a cross-check, an angular distribution measurement was performed. The DCO ratios are extracted from measured γ-ray intensities for certain detector angles according to the following prescription:

$$R_{\mathrm{DCO}} = \frac{I_{24°}^{\gamma_1}(\mathrm{gate}_{63°}^{\gamma_2})}{I_{63°}^{\gamma_1}(\mathrm{gate}_{24°}^{\gamma_2})}, \tag{4.1}$$

where $I_{24°}^{\gamma_1}(\mathrm{gate}_{63°}^{\gamma_2})$ is the intensity of γ_1 at 24° in a spectrum gated by γ_2 detected at 63°, and $I_{63°}^{\gamma_1}(\mathrm{gate}_{24°}^{\gamma_2})$ is the γ_1 intensity from a γ_2-gated projection on the 63° axis. The DCO ratios are compared with calculated values for the given detector geometry. For a stretched quadrupole transition of interest (γ_1), the calculated DCO ratios are $R_{\mathrm{DCO}} = 1.0$ when γ_2 is a stretched $E2$ and $R_{\mathrm{DCO}} = 0.6$ when γ_1 is a pure $\Delta I = 1$ dipole transition. We consider only $E2$ transitions for the $\Delta I = 2$ case, while $\Delta I = 1$ transitions can be either of $M1$ or $E1$ character.

In addition to a DCO analysis, an angular distribution measurement was performed. This was done by projecting the spectra for the individual Ge detectors, finding the areas of the peaks of interest, correcting for the detector efficiency, and fitting the angular intensities to the distribution function:

$$W(\theta) = A_0[1 + Q_2 A_2 P_2(\cos\theta) + Q_4 A_4 P_4(\cos\theta)], \tag{4.2}$$

where Q_k are the solid angle correction coefficients [8], and $P_k(\cos\theta)$ are the Legendre polynomial functions. The four angles available for this measurement were 0°, 24°(156°), 63°(116°) and 87°. The A_2/A_0 and A_4/A_0 coefficients were obtained using a least squares fit of Eq. (4.2) to the experimental data and are listed in Table I. The A_2 values for stretched $E2$ transitions should range between 0.35 and 0.2 and increase smoothly as spin increases. Indeed, the quadrupole transitions exhibit a relatively large increase in the A_2 coefficients as a function of I. The A_4 coefficients for these same $E2$ γ rays should have values ranging from -0.15 at low spins to -0.03 at the highest observed spin levels. While the measured A_4 values have negative values at the lowest spins, they take on positive values at moderate to high spins. The reasons for these small deviations must be due to measurable angular correlations between the Ge detectors. The presence of these correlations, however, does not prevent one from using these data as a cross-check for spin assignments suggested in the DCO data.

Parity assignments for states are determined based on comparison with analogous states in known nuclei. Justification for specific cases are presented below. Specific energies and intensities, as well as DCO and angular correlation values for γ rays associated with ^{183}Au, are listed in Table I.

1. Bands 1–3: Negative-parity structures

A rotational structure has been found to be built on top of the $\frac{9}{2}^-$ level and is labeled as band 1 in Fig. 1. This structure has been established up to the 5500-keV level. Figure 2 shows a spectrum generated by summing the three gates taken on the 571.5-, 627.6-, and 668.9-keV transitions. These gates illustrate band 1 and the γ-ray transitions up to the 735-keV decay. The measured DCO ratios for these transitions (listed in Table I) indicate that the transitions in this band are of $\Delta I = 2$ type and, therefore, $E2$ in nature. DCO values for the two or three highest-energy transitions could not be established and therefore spins are given in parentheses. However, these are likely of $E2$ character as well since the transition energies increase up to the highest spins observed.

Based on DCO measurements, the γ-ray transitions placed in band 2 can also be established as $\Delta I = 2$ electric quadrupole transitions. Band 2 is observed to decay to band 1 predominantly by the 261.4- and 368.7-keV transitions. The measured DCO ratios of 0.74 ± 0.22 and 0.51 ± 0.08 for these two transitions indicate that both of these interband γ rays are of $\Delta I = 1$ mixed dipole/quadrupole multipolarity, thus establishing the spins of the levels in band 2. A negative parity is assigned to this band based on the comparison with a similar band observed in ^{185}Au.

For band 3, it was only possible to obtain DCO ratios for three of the seven transitions observed. The values for these three γ rays indicate that they are $\Delta I = 2$ $E2$ transitions. The other transitions within this band are also assumed to have $E2$ multipolarity. The primary decay out of this band is to bands 1 and 2 and occurs at the 1487.0-keV level via the 498.5- and 464-keV transitions. The measured angular correlations suggest that the three intraband γ rays from band 3 to 2 have a $\Delta I = 2$ character, which establishes the relative spins of levels in band 3 compared with band 2.

Support for the proposed negative-parity assignment to band 3 comes from the observation of the crossover $\frac{27}{2}^- \rightarrow \frac{23}{2}^-$ transition between bands 2 and 3. This cross-talk is indicative of a band interaction, implying that the wave function for the 1544-keV level in band 2 is mixed with the wave function of the 1487-keV level in band 3 and consequently these levels have the same parity.

2. Band 5: Positive-parity structure

The measured DCO ratios for the 163.6–652.9-keV γ rays in band 5[1] indicate that these transitions are $\Delta I = 2$ electric quadrupoles. A spectrum resulting from a gate on three transitions in this cascade is shown in Fig. 3. Decay out of this band is observed to occur at the 701- and 865-keV levels. While a DCO measurement was not possible for the

[1] This band is labeled ''5,'' to be consistent with the level scheme for ^{181}Au (see Sec. V).

TABLE I. γ-ray energies, intensities, and DCO ratios for bands in ^{183}Au. Uncertainty in the γ-ray energies is 0.2 keV when the decimal point is present and 0.5 keV when the decimal point is not present. Intensities of γ-ray transitions are relative to the 283.1-keV transition in band 5. The values in column ''Intensity (converted)'' are the total decay intensity for the given transition, accounting for internal conversion by using the coefficients from Rösel *et al.* [39].

E_γ (keV)	Band	I_γ relative	Intensity (converted)	A_2/A_0	A_4/A_0	R_{DCO}
218.8	1	103±2.5	131.8±3.2	0.390±0.066	−0.15±0.009	1.00±0.07
334.1	1	59.6±0.7	64.1±0.8			1.07±0.13
423.9	1	51.6±1	53.6±1.0	0.509±0.063	−0.10±0.080	
502.8	1	37.9±4	38.9±4.1	0.415±0.108	0.015±0.019	
571.5	1	19.3±3.8	19.7±3.9	0.530±0.100	0.080±0.150	1.00±0.40
627.6	1	16±4	16.2±4.1	0.580±0.140	−0.08±0.210	0.91±0.14
668.9	1	13±4	13.2±4.1	1.020±0.230	0.050±0.280	1.19±0.30
693.1	1	8±4	8.1±4.0	0.720±0.200	−0.38±0.360	1.19±0.59
712.5	1	5±2	5.1±2.0			
735	1	2±1	2.0±1.0			
776	1	1±1	1.0±1.0			
204.4	2	80.6±2	109.0±2.7	0.351±0.065	−0.27±0.140	1.02±0.28
326.1	2	58.6±1	63.3±1.1	0.381±0.056	0.120±0.090	1.02±0.14
423.2	2	25.6±6.2	26.6±6.4	0.509±0.063	−0.10±0.080	0.92±0.25
522	2	15±4	15.4±4.1			
552	2	5±2	5.1±2.0			2.20±0.11
589	2	6±3	6.1±3.1			
625	2	1±1	1.0±1.0			
261.1	2 → 1	35.1±1.1	52.8±1.7	−0.08±0.072	−0.05±0.112	0.74±0.22
368	2 → 1	10.9±0.7	13.1±0.8			0.51±0.08
555	2 → 1	1.8±0.3	1.9±0.3			
609.2	2 → 3	5±2	5.1±2.0			
433.0	3	7.3±0.7	7.6±0.7	0.639±0.240	0.160±0.350	
498.9	3	25.9±1	26.6±1.0	0.169±0.040	0.280±0.800	0.89±0.18
555.1	3	14.3±1.8	14.6±1.8	0.320±0.110	−0.13±0.150	
607.9	3	6.2±0.5	6.3±0.5	0.760±0.100	−0.22±0.170	0.90±0.17
649.5	3	5.5±2	5.6±2.0	0.580±0.140	0.280±0.230	0.92±0.29
662.2	3	3.4±2	3.4±2.0			
668	3	1±1	1.0±1.0			
498.5	3 → 1	13.7±3	14.9±3.3	0.169±0.040	0.280±0.080	
441	3→ 2	17±5	17.6±5.2			1.40±0.40
455	3 → 2	7±3	7.2±3.1			1.30±0.60
464	3 → 2	13.3±2	13.7±2.1	0.463±0.120	−0.02±0.190	1.00±0.30
163.6	5	33.3±3.3	59.0±5.8	0.210±0.267	0.077±0.370	1.12±0.14
283.1	5	100	112.3	0.318±0.171	−0.38±0.090	1.02±0.11
379.2	5	85±2.3	89.5±2.4			0.99±0.15
453.4	5	74.5±5.1	77.0±5.3	0.494±0.056	0.027±0.090	1.05±0.15
509.8	5	72.7±5.6	74.5±5.7	0.688±0.092	0.047±0.134	0.99±0.20
557.8	5	59.4±6.2	60.6±6.3	0.556±0.093	0.083±0.118	1.23±0.40
608.0	5	27.4±3.7	27.9±3.8	0.386±0.082	0.251±0.128	0.90±0.17
652.9	5	14.3±1.8	14.5±1.8	1.009±0.293	0.293±0.246	0.74±0.30
679.6	5	12±1	12.2±1.0	0.563±0.225	0.159±0.311	
692.1	5	6.5±1	6.6±1.0	0.719±0.202	−0.37±0.361	
700.2	5	3±2	3.0±2.0			
729	5	1±1	1.0±1.0			
769	5	1±1	1.0±1.0			
300	5 → 1	10.8±3	11.1±3.1			
265.8	5 → 2	47.8±4.8	49.5±5.0	−0.32±0.171	0.231±0.261	0.58±0.09
428.3	5 → 2	36±3.6	36.4±3.6	−0.74±0.074	0.185±0.096	0.75±0.41

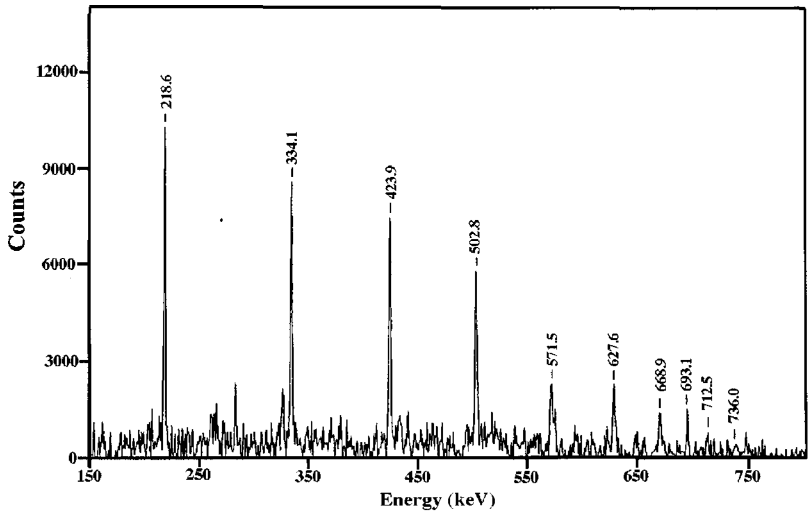

FIG. 2. Representative spectrum illustrating band 1 in ^{183}Au from a sum of gates taken on the 571.5-, 627.6-, and 668.9-keV transtions.

300-keV decay-out γ ray, the 265.8- and 428.3-keV transitions are determined to have ratios (0.58 ± 0.09 and 0.75 ±0.41, respectively) which suggest that these two interband γ rays have $\Delta I=1$ dipole multipolarities. The five transitions above the 4309-keV level in band 5, where the γ rays were too weak for DCO measurements, are assumed to have $E2$ multipolarity. A structure similar to band 5 was observed by Larabee *et al.* [2] in ^{185}Au. The band in ^{185}Au was assigned positive parity. Based on the comparison of this band to ^{183}Au, band 5 is also assigned to have positive parity.

B. ^{181}Au

Analysis of the total and angle-sorted γ-γ-coincidence matrices revealed nine bands or fragments of $E2$ decays. The proposed level scheme for ^{181}Au is shown in Fig. 4. This level scheme represents the first establishment of excited states observed in ^{181}Au. The γ rays following a ^{181}Hg decay and possibly associated with ^{181}Au were reported by Sauvage *et al.* [9]; however, a level scheme was not established and none of the γ rays from that report correspond with the transitions presented here. The measured properties of the newly observed γ rays are listed in Table II. The spins of the levels in ^{181}Au are based on the assumption that the lowest level observed in band 1 has a spin and parity of $I^{\pi}=\frac{9}{2}^{-}$.

This assignment for the spin of the lowest level is based on the systematics between levels observed in ^{181}Au, ^{183}Au, and ^{185}Au. Unlike ^{183}Au, there is no information on the low-energy level structure of ^{181}Au available from decay work and thus we cannot be sure of the $\frac{9}{2}^{-}$ assignment. Nevertheless, this assignment is most likely by comparison with ^{183}Au and ^{185}Au. As with the ^{183}Au experiment, the assignments of spins for the excited states are based on DCO ratio measurements of γ decays. While the number of detectors for the ^{181}Au experiment was greater than that for ^{183}Au, the same angle groups were used (63° and 24°). As a consequence, and DCO ratio of $R_{\rm DCO}=1.0$ is expected for a stretched $E2$ transition and $R_{\rm DCO}=0.6$ for a pure $\Delta I=1$ dipole transition. Unlike the analysis of ^{183}Au, it was determined that an angular distribution analysis was unnecessary for determining spins in ^{181}Au.

1. Bands 1–3: Negative-parity structures

A series of γ-ray transitions is assigned feeding directly into the $\frac{9}{2}^{-}$ state. These γ rays are labeled band 1 in Fig. 4. A gate on the 342.6-keV transition in this band is shown in Fig. 5(a). Three of the γ rays in this band are nearly energetically identical to those in band 2, thus making it difficult or impossible to determine accurate DCO ratios for many of the transitions. Those transitions for which ratios were estab-

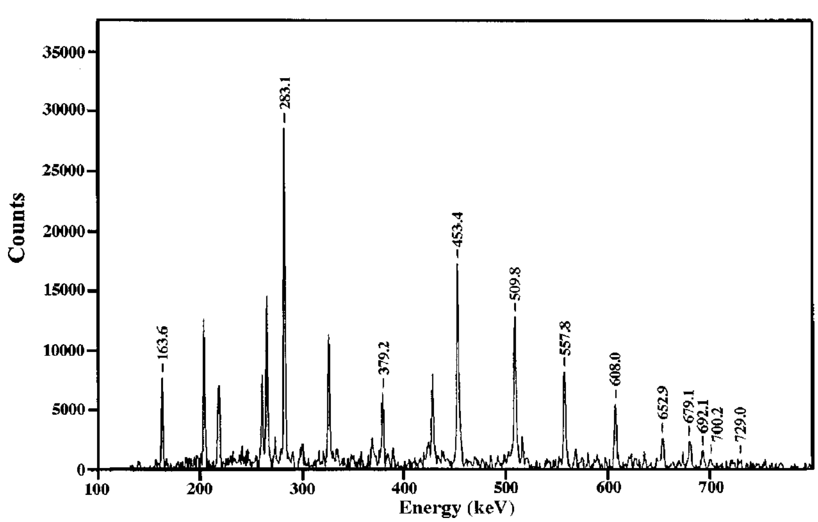

FIG. 3. Representative spectrum illustrating band 5 in ^{183}Au from a sum of gates taken on the 379.2-, 652.9-, and 679.1-keV transtions. Only the members of the band are labeled in the figure.

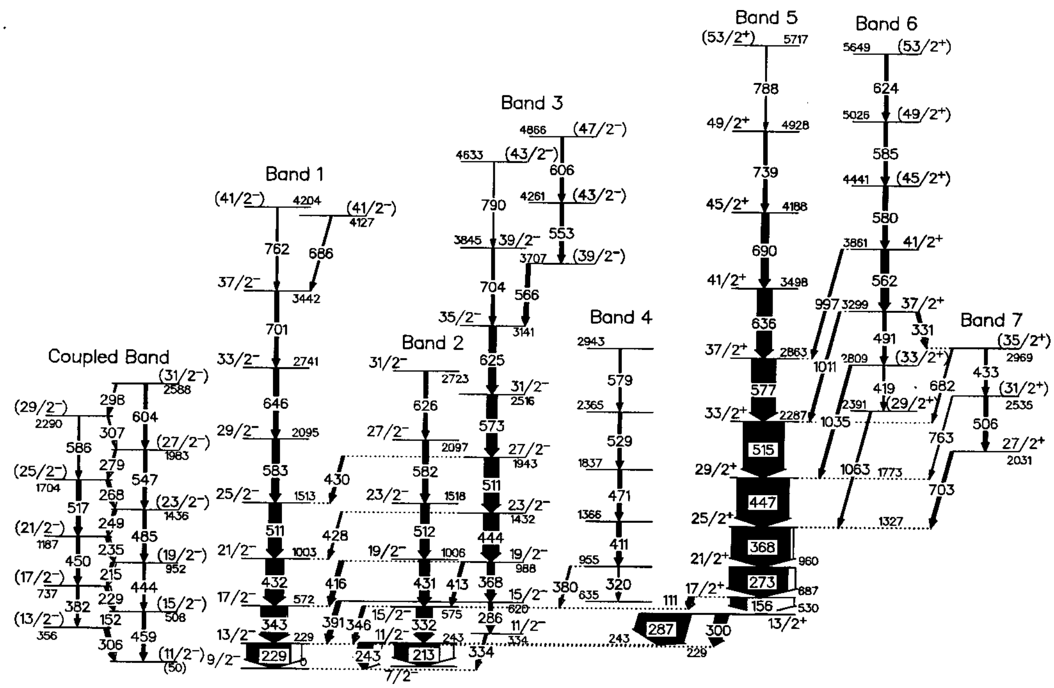

FIG. 4. Level scheme for ^{181}Au. The level energies in bands 1–7 are relative to the $\frac{9}{2}^-$ level in band 1. The energy of the $\frac{11}{2}^-$ level in the coupled band is arbitrarily set to 50 keV, and the energies of the other levels in this band are relative to the energy of $\frac{11}{2}^-$. The widths of the arrows represent the relative intensity of the transitions, and the black and white shading corresponds to the γ-ray (measured) and internal-conversion (calculated) intensities, respectively. Assignments of spin and parity of levels are discussed in the text.

lished confirm that the γ rays are $\Delta I = 2$ quadrupole in character. The multipolarity of the 762-keV and 686-keV transitions feeding in at the top of the band could not be established due to limited statistics.

A representative spectrum for band 2 obtained from a gate on the 331.9-keV transition is shown in Fig. 5(b). This gate indicates not only γ rays in band 2, but also those in band 5 that result from the 111.1-keV transition that feeds from band 5 into band 2. Decays from bands 3 and 4 are also observed in this gate because of the 413.4-keV and 380.4-keV transitions that feed the level directly above the gated γ ray. The 228.9-keV γ ray of band 1 appears in this gate because of the 331.1-keV doublet in band 7. As mentioned in the previous paragraph three of the transitions in band 2 are doublets with γ rays in band 1. Those transitions where DCO measurements are possible exhibit $\Delta I = 2$ quadrupole multipolarity. The spins in this band are fixed by the measured multipolarity of the 242.6-keV transition that connects band 2 to band 1. The DCO ratio for this transition is 0.78 ± 0.04, which is the expected ratio for a $\Delta I = 1$ mixed dipole-quadrupole transition. An assignment of this as a mixed $\frac{11}{2}^- \rightarrow \frac{9}{2}^-$ transition is consistent with this ratio, and agrees well with similar transitions in neighboring nuclei.

The γ-ray transitions in band 3 are clearly established from the gate on the 391.2-keV transition [see Fig. 5(c)], despite the large number of doublets in this band. The 286.5-, 367.7-, and 444.0-keV peaks are all doublets or near doublets with transitions in band 5. The 510.7-keV γ ray is nearly identical to ones in both bands 1 and 2, and the 624.9-keV also has an identical counterpart in band 2. DCO measurements were only possible for three transitions in this band. For γ rays above $35/2^-$, the multipolarities are not known, but are postulated as being $E2$ transitions. There are five transitions identified as decaying from band 3 to band 1. The resulting DCO ratios for the 391.2- and 416.4-keV transitions are below the $\Delta I = 1$ pure dipole value, and indicate that these γ rays have a dipole/quadrupole multipolarity (for $I \rightarrow I-1$) characterized by a large negative mixing ratio.[2] These ratios establish the spins for the levels in band 3, and provide strong indication that the transitions are of $M1/E2$ type, thus fixing the parity as well. A transition is also observed from the $\frac{19}{2}^-$ level in band 3 to the $\frac{15}{2}^-$ level in band 2, and results from the fact that the $\frac{19}{2}^-$ levels of bands 2 and 3 are only 18 keV apart. This interaction between the two bands lends further support for both the parity and spin assignments.

2. Band 4

Band 4 is a set of weak transitions representing about 4% of the total decay intensity of the nucleus. The band is connected with the rest of the level scheme via a 380-keV transition from the level fed by the 411-keV transition. Evidence for this 380-keV transition, as well as several transitions from in this band, can be seen in Fig. 5(b). The γ rays in this band, including the decay-out transition, are too weak to extract DCO ratios; so the spins cannot be deduced. Based on

---

[2]Mixing ratio is defined as

$$\delta(\gamma_n) = k_n \frac{\sqrt{3}}{10} \frac{\langle I_{n+1} || \mathcal{M}(E2) || I_n \rangle}{\langle I_{n+1} || \mathcal{M}(M1) || I_n \rangle},$$

where k_n is the energy of the transition γ_n expressed in units where $\hbar = m = c = 1$. This definition assumes the sign convention used by Krane *et al.* [10].

TABLE II. γ-ray energies, intensities, and DCO ratios for transitions in ^{181}Au. Uncertainty in the γ-ray energies is 0.2 keV when the decimal point is present and 0.5 keV when the decimal point is not present. Intensities of γ-ray transitions are relative to the 272.5-keV transition in band 5. the values in column ''Intensity (converted)'' are the total decay intensity for the given transition, account for internal conversion by using the coefficients from Rösel *et al.* [39].

E_γ (keV)	Band	I_γ relative	Intensity (converted)	R_{DCO}	E_γ (keV)	Band	I_γ relative	Intensity (covered)	R_{DCO}
228.9	1	133.1±1.1	165.2±1.4	0.90±0.04	577.0	5	71.1±2.2	72.4±2.3	0.90±0.06
342.6	1	74.7±2.5	79.9±2.7		635.8	5	43.4±1.4	44.1±1.4	0.95±0.09
431.5	1	51.7±1.8	53.7±1.9	1.19±0.08	690.4	5	20.7±0.8	21.0±0.8	1.10±0.15
510.5	1	36.9±1.6	37.8±1.6		739.2	5	9.7±0.5	9.8±0.5	1.32±0.5
582.6	1	21.1±0.9	21.5±0.9	1.21±0.28	788	5	1.9±0.3	1.9±0.3	
646.4	1	14.0±0.6	14.2±0.6	1.14±0.4	286.7	5→1	149.4±4.7	153.9±4.9	0.76±0.12
700.6	1	10.0±0.5	10.1±0.5	1.75±1.24	111.1	5→2	13.0±0.5	17.1±0.6	0.86±0.02
762	1	3.4±0.3	3.5±0.3		300.4	5→2	35.7±1.2	36.6±1.2	1.02±0.08
686	1	4.6±0.4	4.6±0.4		419	6	4.4±0.3	4.5±0.3	
213.2	2	138.6±4.5	181.0±5.9	0.90±0.1	490.7	6	9.9±0.5	10.2±0.5	
331.9	2	45.2±1.8	48.7±1.9	0.92±0.05	562.5	6	21.5±0.8	21.9±0.8	1.20±0.2
431.4	2	28.6±1.4	29.6±1.4	1.07±0.16	579.9	6	13.0±0.6	13.3±0.6	
512.3	2	24.3±1.1	24.9±1.1	0.83±0.32	585.2	6	10.5±0.5	10.6±0.5	
582.2	2	15.4±0.9	15.7±0.9	1.81±0.4	624	6	8.7±0.5	8.8±0.5	
626.4	2	10.1±0.6	10.2±0.6	1.03±0.54	996.8	6→5	5.7±0.4	5.7±0.4	2.61±1.5
242.6	2 →1	43.8±0.0	70.7±0.0	0.78±0.04	1010.7	6→5	6.8±0.4	6.8±0.4	1.14±0.6
345.6	2 →1	8.8±0.6	10.8±0.7		1035.2	6→5	8.6±0.5	8.7±0.5	
286.5	3	11.1±0.7	12.4±0.7		1063	6→5	4.9±0.4	4.9±0.4	
367.7	3	21.0±1.0	22.2±1.1		331.1	6→7	8.2±0.4	10.3±0.6	
444.0	3	44.4±1.6	46.0±1.7	1.26±0.4	432.6	7	8.6±0.6	8.9±0.6	
510.7	3	41.8±1.7	42.8±1.7		506.2	7	11.1±0.6	11.4±0.6	
553.2	3	8.7±0.5	8.8±0.5		682	7→5	4.2±0.4	4.4±0.4	
566.1	3	11.0±0.5	11.2±0.5		703.5	7→5	9.5±0.6	9.8±0.6	0.47±0.3
573.1	3	29.7±1.1	30.3±1.1	1.69±0.4	763	7→5	3.4±0.4	3.5±0.4	
605.7	3	7.9±0.5	8.1±0.5		153.1	C.B.	4.2±0.5	9.7±1.1	
624.9	3	21.9±0.9	22.2±0.9	0.64±0.8	215.5	C.B.	8.3±0.5	15.5±0.9	
703.8	3	7.6±0.5	7.7±0.5		228.7	C.B.	9.9±0.7	17.1±1.3	
790	3	1.5±0.3	1.6±0.3		232.1	C.B.	3.8±0.3	±	
334.0	3→1	5.0±	6.3±0.0		234.8	C.B.	7.6±0.4	12.8±0.7	
391.2	3→1	12.0±0.7	14.0±0.8	0.37±0.1	250.2	C.B.	6.8±0.4	10.7±0.6	
416.4	3→1	11.5±0.5	13.1±0.6	0.34±0.4	267.1	C.B.	7.1±0.4	10.4±0.6	
428	3→1	4.5±0.6	5.1±0.7		280.5	C.B.	4.5±0.3	6.3±0.5	
430	3→1	7.4±0.7	8.3±0.8		297	C.B.	3.4±0.3	4.6±0.4	
413.4	3→2	8.2±0.5	8.5±0.5		305.4	C.B.	6.0±	8.0±0.0	
319.9	4	3.1±0.6	3.3±0.6		308	C.B.	2.8±0.3	3.6±0.4	
411.4	4	11.5±0.8	12.0±0.8		381.6	C.B.	5.9±0.6	6.2±0.6	
471.3	4	10.8±0.6	11.1±0.6		444	C.B.	6.5±0.7	6.7±0.7	
528.7	4	10.2±0.5	10.4±0.6		450.3	C.B.	10.2±0.7	10.5±0.7	
578.9	4	5.4±0.5	5.4±0.5		458.6	C.B.	7.9±1.1	8.1±1.1	
380.4	4→2	3.4±0.6	4.0±0.7		484.7	C.B.	8.6±0.6	8.9±0.6	
156.3	5	101.1±3.2	191.9±6.0	0.89±0.02	516.7	C.B	11.6±0.7	11.8±0.7	
272.5	5	177.4±5.4	201.9±6.2	1.04±0.02	547.4	C.B.	9.6±0.6	9.8±0.6	
367.5	5	178.0±5.4	188.3±5.7	1.04±0.02	586	C.B.	4.6±0.6	4.6±0.6	
446.7	5	151.9±4.6	157.1±4.8	1.11±0.03	604	C.B.	8.7±0.7	8.8±0.7	
514.9	5	120.3±3.7	123.2±3.8	0.95±0.03					

the energy spacing the in-band transitions are likely stretched $E2$'s of a collective rotational band.

3. Bands 5–7: Positive-parity structures

For excitation energies $500 < E_x < 2000$, the γ rays in band 5 are the most intense transitions in the nucleus. DCO ratios measured for the transitions in band 5 clearly indicate that the γ rays have $E2$ multipolarity. Figure 6(a) shows the spectrum from a gate on the 272.5-keV γ ray. Visible in this gate are the 111.1-, 286.5-, and 300.4-keV transitions that decay out of band 5 into bands 2 and 1. The 111.1- and 286.5-keV γ rays have DCO ratios of 0.86 and 0.76, respectively. These values indicate that the two transitions have primarily $\Delta I = 1$ dipole multipolarity. This would set the lowest spin of band 5 as $\frac{13}{2}$. Further support for this assignment comes from the DCO measurement of the 300.4-keV transition from band 5 to band 1. This transition has a ratio of 1.02 ± 0.08. Such a ratio indicates either a $\Delta I = 2$ quadru-

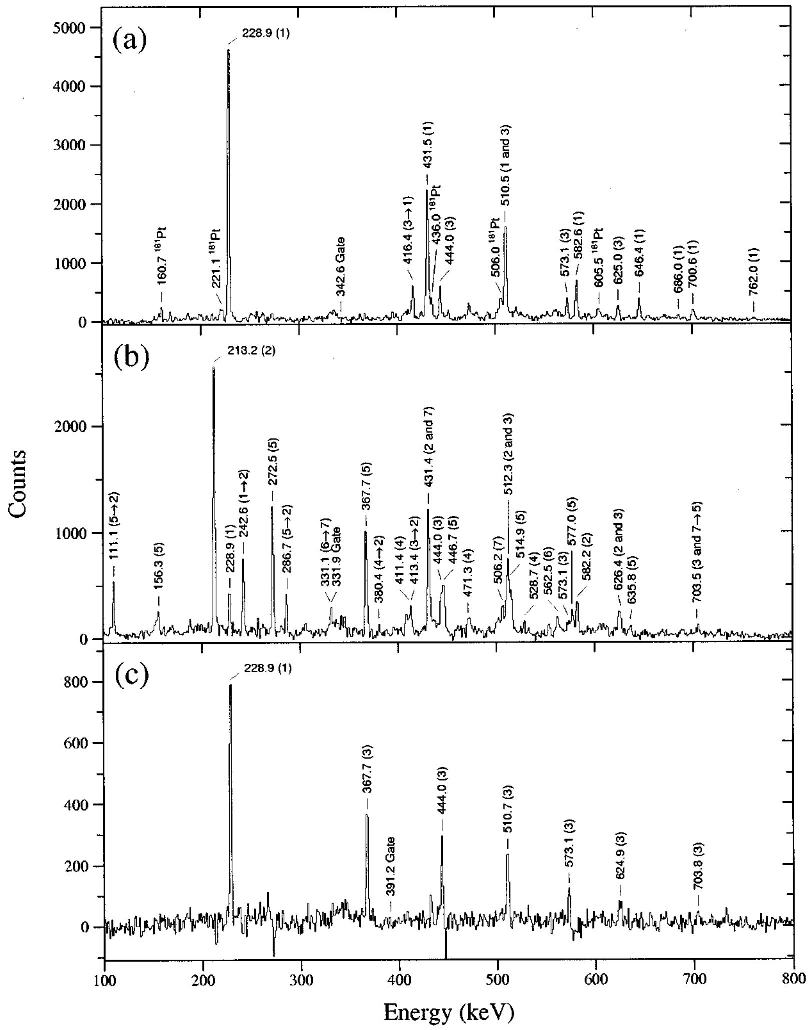

FIG. 5. Representative coincidence spectra illustrating bands 1, 2, and 3 in ^{181}Au with gates on the (a) 342.9-keV, (b) 331.9-keV, and (c) 391.2-keV transitions, respectively. The values in parentheses following the peak marker indicate the band (see Fig. 4) in which the γ-ray transition is found.

pole transition or a dipole distribution of a γ ray connecting two levels of the same spin. Since the 300.4-keV transition feeds the $\frac{13}{2}^-$ level of band 1, an assignment of $\frac{13}{2}$ for the spin of the lowest level in band 5 is consistent with the ratios for all three decay-out transitions. Structures similar to band 5 in ^{181}Au are also observed in ^{183}Au and ^{185}Au. Based on the comparison of these bands with bands in ^{181}Au, band 5 is also assigned positive parity. From the spin assignments, it is clear that band 5 is the yrast sequence for spins $\frac{21}{2}$ and greater.

Sidebands like 6 and 7 feeding the positive-parity yrast band are observed for the first time in Au nuclei. The transitions in band 6 and 7 are clearly seen in Fig. 6(b). The 562.5-keV transition in band 6 is the only transition in this band where a DCO measurement is possible, and its value is consistent with a $\Delta I=2$ quadrupole assignment. Band 6 is connected with band 5 by four γ-ray transitions with energies $\sim$1 MeV. These transitions are clearly observed in the gate of the 272.5-keV γ ray in band 5. The peaks are shown in the inset of Fig. 6(a). For the 1010.7-keV and 996.8-keV γ rays, a DCO measurement was possible; however, the uncertainties are large. These transitions have ratios of 1.14 ± 0.6 and 2.61 ± 1.5, respectively. These values are consistent with the transitions being $\Delta I=2$ quadrupoles or $\Delta I=0$ dipoles. The quadrupole multipolarity was chosen based on comparison of the intensities of the γ decays at the highest levels in band 5 with those of band 6. With the spins indicated for band 6 in Fig. 4, the 5649-keV level is the yrast level for $I=\frac{53}{2}$. This is consistent with the fact that for spins $>\frac{45}{2}\hbar$, band 6 is more intense than band 5. In heavy-ion fusion reactions the yrast levels are typically the most strongly populated.

For band 7, decay-out transitions from all three levels have been established. Multipolarity measurements were not possible for the 506- and 433-keV transitions, but the relative spin for band 7 is established by measured DCO ratio for the 703.5-keV decay-out transition. This ratio, 0.47 ± 0.30, suggests that the 703.5-keV γ ray corresponds to a $\Delta I=1$ transition. The 703.5-keV transition, together with 763- and 682-keV γ rays, has the appearance of the decay-out of a band of which only the 433- and 506-keV members are observed. Based on this appearance, a likely assignment for the 763- and 682-keV γ rays is $M1$ and the 433- and 506-keV transitions $E2$. This leads to the proposed spin assignments for the $E_x=2535$ and 2969 keV levels in band 7 to be $I=\frac{31}{2}$ and $\frac{35}{2}$, respectively. The fact that the in-band transitions do not show the typical rotational behavior can be explained in terms of perturbation with other levels of similar spin. This interpretation is discussed further in Sec. V C.

4. Coupled band

A previously unobserved strongly coupled band has also been identified. This band has the same dependence total

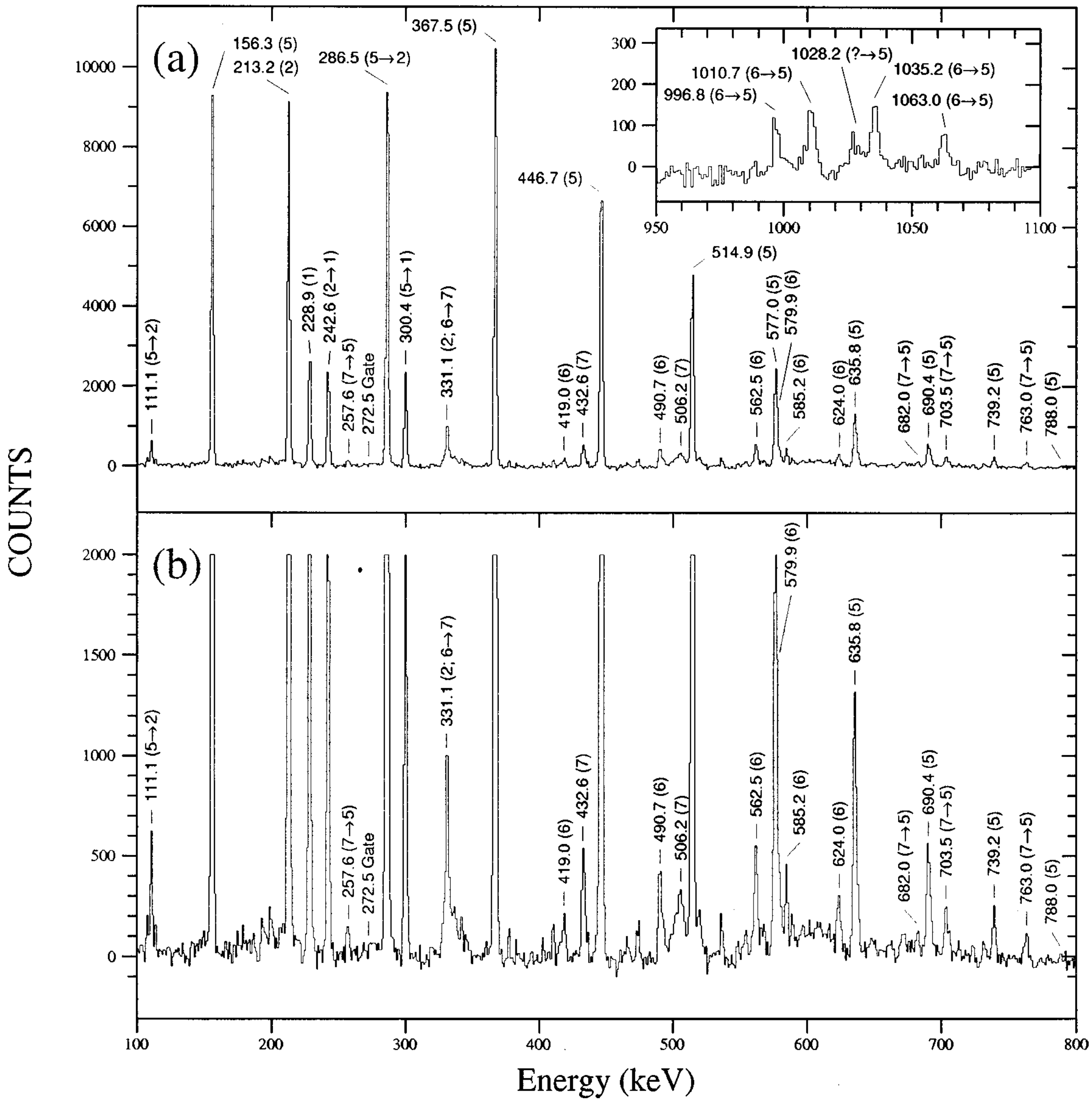

FIG. 6. Representative coincidence spectrum illustrating bands 5, 6, and 7 in ^{181}Au with a gate on the 272.5-keV transition. Panel (a) has a full scale y axis to emphasize transitions in band 5, while (b) has a restricted scale y axis to observe band-6 and -7 γ-ray lines. Inset: Spectral range of this projection is around 1 MeV to highlight linking transitions from band 6 to 5. The values in parentheses following the peak marker indicate the band from Fig. 4 in which the γ-ray transition is found.

energy (H) and fold (K) of the Spin Spectrometer as other bands in ^{181}Au and is assigned to the decay of this nucleus. No connecting transitions have been observed that establish the relative excitation energy or spin of the ''coupled band'' with the other levels in ^{181}Au. Thus the excitation energy of the levels in this band is based on the lowest level being arbitrarily set to 50 keV. The spin assignments of the levels are postulated from arguments made in Sec. V D.

V. CONFIGURATION ASSIGNMENTS

All four bands observed in ^{183}Au (see Fig. 1) can be shown to have a configuration that corresponds to a like band in ^{181}Au (Fig. 4). These corresponding bands have been given the same label in their respective level schemes to illustrate their connection (e.g., band 1 in both ^{183}Au and ^{181}Au can be interpreted as being based on a $\pi h_{9/2}$ configuration). The interpretation of these bands also follows a similar rationale. Because of this, the following discussion of the configuration assignments of the respective bands is done together for these two nuclei.

Prolate and oblate shapes coexisting in the same nucleus have been identified in several Pt and Hg nuclei around $N=108$. Systematic studies of the even-even Pt nuclei (e.g., Ref. [11]) indicate that the ground states of Pt nuclei around from $N=100$ to 108 are prolate. Likewise, prolate configurations in even-even Hg are also minimum in energy (although not the ground state) around $N=104$. Shape coexistence has also been observed in ^{185}Au [2] and ^{187}Au [3], and examination of the trend in heavier Au nuclei (see, e.g., Ref. [1]) provides a clear indication that the level structures observed in ^{183}Au and ^{181}Au originate from prolate deformed configurations. Decoupled bands resulting from $\pi h_{9/2}$, $\pi f_{7/2}$, and $\pi i_{13/2}$ valence protons coupled to a prolate core were established in ^{185}Au [2]. Potential-energy–surface calculations [12] indicate that corresponding prolate states in

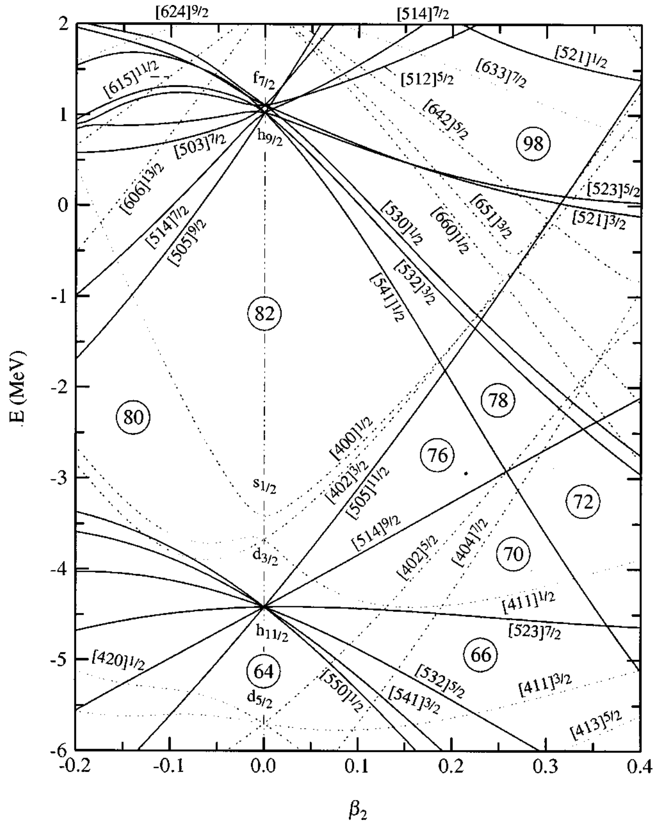

FIG. 7. Deformed single-proton level diagram around $Z=79$ calculated with the Woods-Saxon potential with $\beta_4=\gamma=0$.

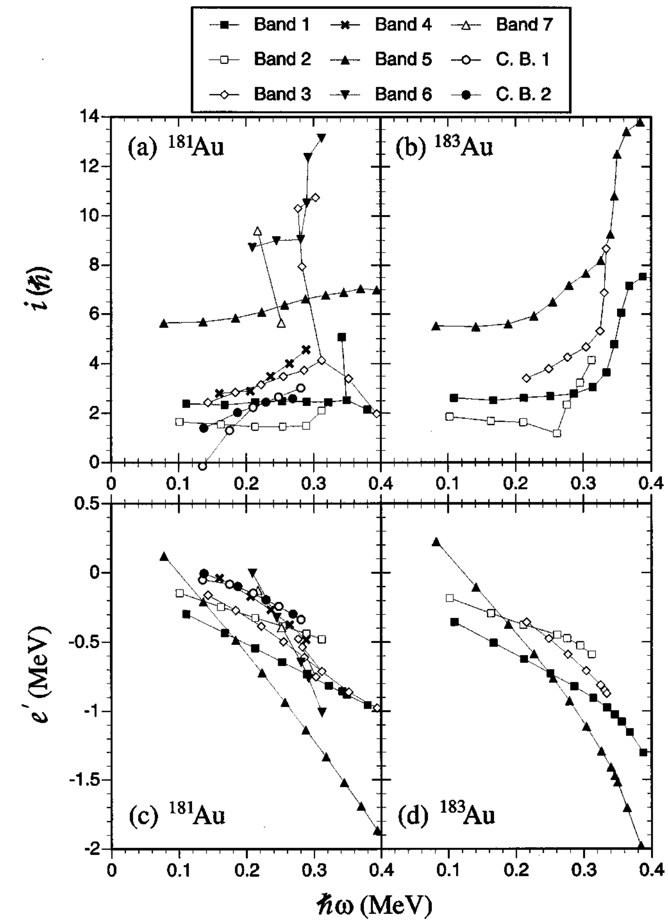

FIG. 8. Extracted alignment and Routhian energy for measured rotational bands in ^{181}Au [panels (a) and (c), respectively], and ^{183}Au [panels (b) and (d)]. The labels in the legends indicate the bands as they are labeled in Figs. 1 and 4. The Harris reference parameters are chosen to be $\mathcal{J}_0=29.4\hbar^2$/MeV and $\mathcal{J}_1=121\hbar^4/\mathrm{MeV}^3$ such that the alignment of band 1 in ^{181}Au is approximately flat.

^{183}Au and ^{181}Au have deformations of $\beta_2\sim 0.2-0.3$. The expected single-particle states for these nuclei can be seen in Fig. 7 as those orbitals around the gap labeled ''78.'' Specifically, single-particle orbitals that are expected to play a role are negative-parity $\frac{1}{2}[541]$, $\frac{3}{2}[532]$, $\frac{1}{2}[530]$, and $\frac{11}{2}[505]$ and the positive-parity $\frac{1}{2}[660]$ configurations. Specific spectroscopic assignments for individual bands are discussed in the following sections.

For the following discussions it is useful to consider the quasiparticle alignment and Routhian energies of the rotational bands. The experimental quasiparticle alignment is calculated as $i=I_x-I_{\mathrm{ref}}$, where $I_x=\sqrt{I(I+1)-K^2}$, and $I_{\mathrm{ref}}=\omega\mathcal{J}_{\mathrm{ref}}(\omega)$. The function $\mathcal{J}_{\mathrm{ref}}(\omega)$ is a frequency-dependent moment of inertia term introduced by Harris [13]: $\mathcal{J}_{\mathrm{ref}}(\omega)=\mathcal{J}_0+\omega^2\mathcal{J}_1$, where $\mathcal{J}_0$ and $\mathcal{J}_1$ are parameters fit to the data. Likewise, the quasiparticle Routhian is $e'=E'-E_{\mathrm{ref}}$, where $E'=E-\omega I_x$, and $E_{\mathrm{ref}}=-\int I_{\mathrm{ref}}\,d\omega=-\frac{1}{2}\omega^2\mathcal{J}_0-\frac{1}{4}\omega^4\mathcal{J}_1+1/8\mathcal{J}_0$. The experimental rotational frequency (ω) is calculated:

$$\omega=\frac{dE}{dI_x}=\frac{E(i)-E(f)}{I_x(i)-I_x(f)}.$$

The resulting calculations of quasiparticle alignment and Routhian energy for all bands observed in the nuclei are plotted vs rotational frequency in Fig. 8.

A. Bands 1–3: $\pi h_{9/2}$-$\pi f_{7/2}$ configurations

Experiments on ^{185}Au [7,2,14] have clearly identified that the lowest negative-parity positive-signature rotational band[3] observed in this nucleus is based on a primarily $\pi h_{9/2}$ quasiparticle configuration. Other low-lying rotational bands identified in these nuclei are based on the negative-signature $\pi h_{9/2}$ configuration and the positive-parity $\pi i_{13/2}$ orbital. The lowest levels of the rotational bands based on these configurations are illustrated in Fig. 9. From a comparison of these bands in ^{185}Au with low-lying states in ^{183}Au and ^{181}Au, band 1 in these two nuclei can also be associated with the $\pi h_{9/2}$ quasiparticle configuration. The alignment and Routhian energies of these bands, denoted by the solid squares in Fig. 8, also support this assignment. From angular momentum coupling rules [15], the lowest signature of a decoupled $\pi h_{9/2}$ rotational band would be $\alpha=+\frac{1}{2}$. By examining the Routhian energies in Figs. 8(c) and 8(d), one can see that band 1 is the lowest-energy negative-parity band

[3]These bands are characterized by the spins and parities $I^\pi=\frac{9}{2}^-,\ \frac{13}{2}^-,\ \frac{17}{2}^-,\ \ldots$.

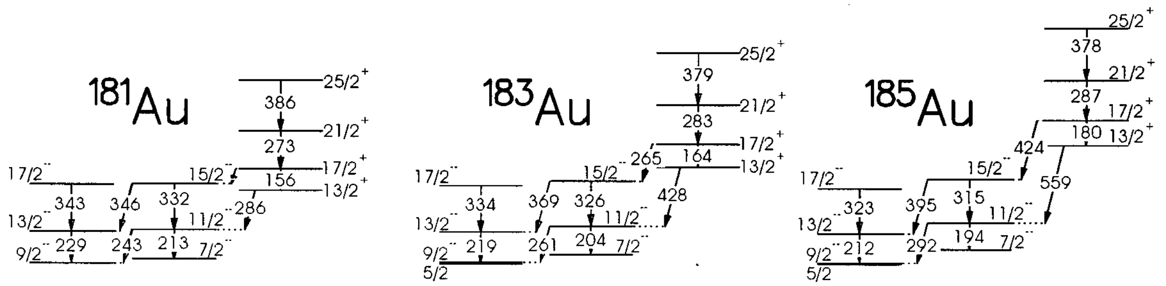

FIG. 9. Partial level schemes of ^{185}Au, ^{183}Au, and ^{181}Au. The excitation energy (E_x) of the $\frac{9}{2}^-$ level above the $\frac{5}{2}^-$ ground state for ^{185}Au and ^{183}Au is denoted in the figure.

observed. Based on our spin assignments, band 1 has a signature of $\alpha=+\frac{1}{2}$, which clearly conforms to the energetically favored signature of the $\pi h_{9/2}$ configuration.

There are two negative-parity $\alpha=-\frac{1}{2}$ rotational bands (bands 2 and 3) that have been identified in both ^{183}Au and ^{181}Au. The alignment and Routhian energy for these two bands are shown as open squares and diamonds in Fig. 8. It is clear that neither can be associated with high-K configurations such as prolate $\pi h_{11/2}$ or oblate $\pi h_{9/2}$ (see Fig. 7), because of the decoupled nature of these two bands. Possible configurations must be related to the prolate $\pi h_{9/2}$ or $\pi f_{7/2}$ orbitals. The energetically favored signature of the $\pi f_{7/2}$ band has $\alpha=-\frac{1}{2}$; this and the unfavored $\pi h_{9/2}$ configuration are possible configurations for bands 2 and 3. Rotational structures similar to bands 2 and 3 have also been observed in ^{185}Au, and an interpretation [2] of the bands in this nucleus was indeed that one is the unfavored signature $\pi h_{9/2}$ while the second structure is related to $\pi f_{7/2}$. The bands identified as the unfavored $\pi h_{9/2}$ bands in ^{185}Au and ^{183}Au are illustrated in Fig. 9. Based on the comparison of the unfavored $\pi h_{9/2}$ band in ^{185}Au to band 2 in ^{183}Au and ^{181}Au, it is clear that such an assignment for band 2 can also be made. By analogy, band 3 can be established as a rotational band based on the $\pi f_{7/2}$ configuration. Because of the close proximity in energy of the $h_{9/2}$ and $f_{7/2}$ spherical shell states,[4] the corresponding deformed single-particle configurations of rotational bands from these orbitals are heavily mixed. As a result, special consideration is taken for the examination of other properties, such as branching ratios and band interaction, for these two bands in Sec. VI B.

As can be seen in Figs. 8(a) and 8(b), a large increase in alignment at $\hbar\omega\approx0.32-0.33$ MeV in ^{183}Au and ^{181}Au is observed in bands 1 and 3. An increasing alignment is also observed in band 2 of ^{183}Au as well as an indication that the alignment of band 2 in ^{181}Au may be starting a significant increase. This dramatic change in alignment is related to the well-known breaking of a pair of $i_{13/2}$ neutrons and subsequent arrangement of their spins along the axis of rotation.

B. Band 4

Because of the smaller resolving power of the Ge setup in the ^{183}Au experiment compared to ^{181}Au, a band corresponding to band 4 in Fig. 4 was not observed in ^{183}Au. The weak intensity and lack of spin assignments for band 4 make the spectroscopic assignment of this band difficult. Since this band feeds the negative-parity band 2 rather than the positive-parity yrast-structure band 5, it is likely that band 4 has negative parity. The alignment and Routhian energy are extracted for band 4 assuming $K=\frac{1}{2}$ and the spin of the lowest level is $\frac{13}{2}$. The results are shown as crosses in Figs. 8(a) and 8(c). As can be seen in the figure, the alignment of band 4 is gradually increasing with respect to the chosen reference and has a value at high rotational frequency that is larger than all other negative-parity states. From the Routhian energy, it may be possible that this band is the signature partner of band 3. The larger alignment of band 4 compared to 3 is probably a result of a larger interaction strength in the $\nu i_{13/2}$ crossing. The absence of transitions between bands 4 and 3 is not understood.

C. Bands 5–7: $\pi i_{13/2}$ band and side bands

The extracted alignment and Routhian energies for bands 5, 6, and 7 are displayed as triangles in Fig. 8. The alignment at $\hbar\omega=0$ of band 5 in ^{181}Au is $\approx5.5\hbar$. If only one-quasiparticle configurations are considered, the only orbital close enough to the ^{181}Au Fermi level with sufficient alignment is $\pi i_{13/2}\ \frac{1}{2}[660]$. The low-lying positive-parity rotational band observed in ^{185}Au has been demonstrated as arising from this orbital. Based on the alignment and comparison with similar bands in heavier Au nuclei, it is clear that band 5 in ^{183}Au and ^{181}Au is based on the one-quasiparticle $\frac{1}{2}[660]$ orbital, as opposed to a multiquasiparticle excitation.

As with band 4, structures corresponding to bands 6 and 7 in ^{181}Au have not been observed in ^{183}Au. Excluding one point in band 7, band 6 has the largest aligned angular momentum below $\hbar\omega=0.25$ MeV with a value of $\approx8.0\hbar$. As observed in bands 1 and 3, band 6 also appears to be influenced by the breaking of a pair of $i_{13/2}$ neutrons. In view of such a large alignment, band 6 must be based on a configuration of at least three quasiparticles. Bark *et al.* [16] reported several positive-parity three-quasiparticle bands in ^{177}Re. In that report, the suggested configurations all involved an $i_{13/2}$ neutron. Since a backbend occurs at a similar rotational frequency as the $\nu i_{13/2}$ alignment in bands 1 and 3, the $\nu i_{13/2}$ orbital is not part of the low-ω configuration of band 6. This is due to the fact that a one-quasiparticle occupation of the lowest $\nu i_{13/2}$ state would inhibit the normal $\nu i_{13/2}$ alignment from occurring at the expected rotational frequency. This well-known blocking effect can be seen in odd-N nuclei throughout the rare-earth region. For this reason the configuration of band 6 being based on a $\nu i_{13/2}$ or-

[4]This proximity can be seen theoretically in Fig. 7 at $\beta_2=0.0$.

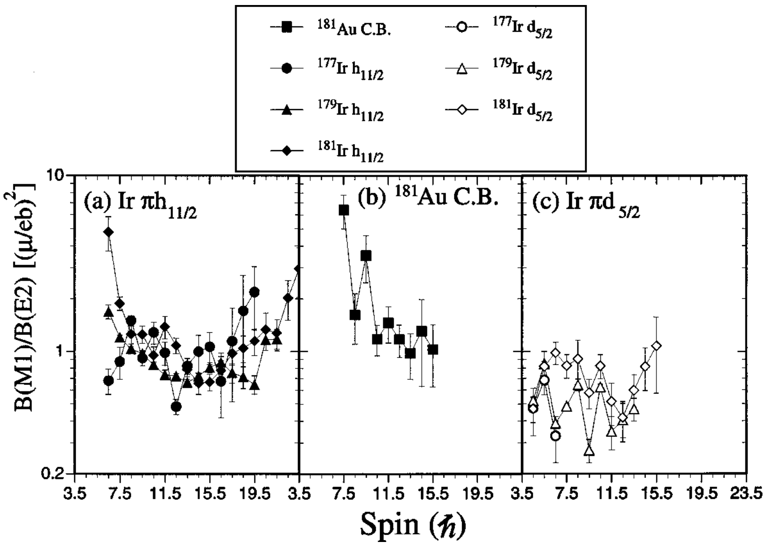

FIG. 10. Measured $B(M1)/B(E2)$ values for (a) $\pi h_{11/2}$ band in ^{177,179,181}Ir, (b) the coupled band in ^{181}Au, and (c) $\pi d_{5/2}$ bands also in ^{177,179,181}Ir. References are provided in the text.

bital is unlikely. A possible configuration for band 6 is a rotational band built on the $\pi\frac{1}{2}[660]\otimes\nu\frac{1}{2}[521]\otimes\nu\frac{5}{2}[512]$ set of single-particle excitations. Rotational bands based on $\nu\frac{1}{2}[521]$ and $\nu\frac{5}{2}[512]$ orbitals have been observed experimentally in $N=103$ ^{181}Pt [17]. The $\frac{1}{2}[521]$ orbital is observed to be the ground-state configuration in ^{181}Pt, and the $\frac{5}{2}[512]$ orbital is observed at an excitation energy of 166.8 keV. Thus, these orbitals would be expected to be energetically favorable in $N=102$ ^{181}Au. Additional support for this assignment comes from the comparison of the signature quantum number (α). The energetically favored signatures for these two configurations as well as the $\pi\frac{1}{2}[660]$ orbital are $\alpha(\nu f_{5/2})=+\frac{1}{2}$, $\alpha(\nu f_{7/2})=-\frac{1}{2}$, and $\alpha(\pi i_{13/2})=+\frac{1}{2}$. From the addition of these values, the favored signature for this configuration would be $\alpha=+\frac{1}{2}$, which corresponds to the observed signature of band 6. Most of the alignment would be contributed by the $\pi i_{13/2}$ state ($\sim 5.5\hbar$), while a small amount would be added by the $\nu f_{5/2}$ and $\nu f_{7/2}$ orbitals. Both the $\frac{1}{2}[660]$ and $\frac{1}{2}[521]$ configurations have a large signature splitting, but there is no splitting observed for the $\frac{5}{2}[512]$ configuration in ^{181}Pt. Thus the signature splitting of band 6 should be determined by the $\frac{5}{2}[512]$ quasineutron, and so one would expect that the signature partner would be observed as well. This, however, is not the case. The likely reason why the signature partner is not observed is that the intensity of this band is too weak to be resolved with this specific set of data.

Only three levels are observed in band 7. It can be seen in Fig. 8(a) that this band is observed in the midst of an apparent backbend. The frequency where this backbend occurs ($\hbar\omega\approx 0.24$ MeV) is too low to be easily considered a $\nu i_{13/2}$ alignment. Rather than a quasiparticle alignment, another consideration is that some of these levels are perturbed by unobserved states, thus causing an appearance of a backbend. If this is the case, band 7 could be interpreted as the unfavored signature of the $\pi i_{13/2}$ band (band 5). Band 7 has an excitation of about 500 keV above band 5 in the Routhian energy plot, Fig. 8(c). This is a comparable energy splitting to that seen in low-K $\nu i_{13/2}$ bands reported in Ref. [18]. A possible source of the perturbation would be from the unobserved signature partner of band 6. Based on the excitation energies of the $33/2^+$ and $37/2^+$ states (2809 and 3299 keV, respectively), the expected energy of the $35/2^+$ level in the (strongly coupled) signature partner would be ~ 3050 keV. This is less than 100 keV from the observed $35/2^+$ level in band 7; thus the perturbation in this band is likely the result of an accidental near degeneracy with a level that is the unseen partner of band 6. This interaction would also explain why a decay is observed from the 3299-keV level in band 6 to the 2969-keV level in band 7. Without additional information on band 7 further conclusions cannot be drawn.

D. Coupled band: $\pi h_{11/2}$ band

Possible spectroscopic assignments for the strongly coupled band in ^{181}Au arise from consultation of the proton single-particle diagram of Fig. 7. Such configurations include the oblate $\frac{9}{2}[505]$ state, as well as the prolate $\frac{11}{2}[505]$ and $\frac{3}{2}[402]$ orbitals. Rotational bands resulting from oblate $\pi h_{9/2}$ orbitals have been observed as the yrast structures of most neutron-deficient odd-A Tl nuclei [19–22]. From total Routhian surface calculations by Wyss *et al.* [23], these configurations in Tl are predicted to have a β_2 parameter of ~ 0.15 (oblate). The energy of γ-ray transitions observed in these bands are on the order of 700 keV for the stretched $E2$'s. The oblate $\pi h_{9/2}$ configuration in Au nuclei is predicted to have a deformation similar to that of Tl; thus one would expect γ-ray transition energies to also be the same order. The transitions in the coupled band of ^{181}Au, however, have energies $\sim 0.6E_\gamma(\mathrm{Tl})$; thus the oblate $\frac{9}{2}[505]$ can be ruled out as a possible configuration.

To aid in the determination of whether the coupled band is prolate $\pi h_{11/2}$ or $\pi d_{5/2}$, one can compare the extracted $B(M1)/B(E2)$ ratios for this band with strongly coupled bands in odd-A Ir nuclei. The resulting $B(M1)/B(E2)$ ratios for the coupled band in ^{181}Au are shown in Fig. 10(b), as well as the $\pi h_{11/2}$ and $\pi d_{5/2}$ bands observed in ^{177}Ir [24], ^{179}Ir [25], and ^{181}Ir [26] in Figs. 10(a) and 10(c), respectively. The $B(M1)/B(E2)$ ratio was extracted from reported γ-ray energies and intensities using the expression

$$\frac{B(M1;I\to I-1)}{B(E2;I\to I-2)}=0.693\frac{E_\gamma^5(I\to I-2)}{E_\gamma^3(I\to I-1)}\frac{1}{\lambda(1+\delta^2)}\ [\mu/e\ \mathrm{b}]^2, \tag{5.1}$$

where E_γ are the γ-ray energies in MeV, λ is the $E2$ to $M1$ branching ratio $[=I_\gamma(I\rightarrow I-1)/I_\gamma(I\rightarrow I-2)]$, and δ is the $E2/M1$ mixing ratio in the $\Delta I=1$ transition. For the calculations, the mixing ratio δ is assumed to be zero.

The values for the coupled band in ^{181}Au are plotted in Fig. 10, assuming the spin of the lowest level is $\frac{11}{2}\hbar$ as denoted in Fig. 4. Motivation for this spin assignment is discussed below. It should be noted that the $B(M1)/B(E2)$ ratio is independent of the relative angular momentum of the band; thus the choice of spin will only shift the ''^{181}Au C.B.'' trend in Fig. 10 left or right. It can be seen in this figure that the $\pi h_{11/2}$ configurations in Ir have ratios of $\approx 1(\mu/e\ \mathrm{b})^2$. The $\pi d_{5/2}$ orbitals show a bit more scatter but have consistently lower $B(M1)/B(E2)$ ratios than the $\pi h_{11/2}$ states. The extracted ratios for the coupled band in ^{181}Au, indicated by the solid squares, have values that are comparable to the $\pi h_{11/2}$ bands in Ir. This provides support for the assignment of the coupled band as the $\pi h_{11/2}$ configuration. Additional confirmation for this assignment comes from the observation of the prolate $\pi h_{11/2}$ band in ^{185}Au [2]. In this case, the strongly coupled prolate band was observed interacting with a lower-lying oblate band based on the $\pi h_{11/2}\ \frac{1}{2}[550]$ orbital.

Figures 8(a) and 8(c) show the calculated alignment and Routhian energy for the coupled band where the two sequences of stretched $E2$ transitions are denoted by open and solid circles. These calculations were made assuming the initial spin is $\frac{11}{2}$ and the excitation energy is arbitrarily set to 50 keV. ''C.B. 1'' denotes the $\alpha=-\frac{1}{2}$ band $(I=\frac{11}{2},\frac{15}{2},\ldots)$, while ''C.B. 2'' the $\alpha=+\frac{1}{2}$ band $(I=\frac{13}{2},\frac{17}{2},\ldots)$. It is evident from this figure that the coupled band shows deviations from strong coupling at both high and low rotational frequencies. The deviations at the high frequencies are possibly a result of the uncertainty of the placement of the γ rays for these weakest transitions. The deviations at low rotational frequencies can be interpreted as arising from the perturbation of these levels by the unobserved oblate $\pi h_{11/2}$ orbital.

It was demonstrated by Wood *et al.* [11] that the lowest members of the ground-state rotational band in ^{180}Pt are perturbed by mixing of prolate and oblate configurations. This perturbation is clearly evident in the quasiparticle Routhian energy of this band. Figure 11 shows the calculated Routhian energy of the ground-state band of ^{180}Pt as triangles. A reference was chosen such that the energies of the high-spin levels before the backbend are approximately flat as a function of rotational frequency. A horizontal line is drawn to illustrate the deviation of the lowest points for ^{180}Pt. As denoted in the figure, the deviation of the lowest point from the reference line is $\sim$0.040 MeV. Also shown in Fig. 11 are Routhian energies of the two stretched $E2$ sequences of the coupled band in ^{181}Au. This band is sloped because of the alignment of the unpaired proton in Au; nevertheless, a straight line can be traced through the points as a common reference. The deviation of the lowest point in ''C.B. 1'' from the coupled band reference line is $\sim$0.045 MeV. It can be seen that the positive signature of the coupled band, ''C.B. 2,'' is not perturbed. The oblate $\pi h_{11/2}$ state is low K and thus would produce a decoupled rotational band. For $\pi h_{11/2}$, the energetically favored signature would be $\alpha=-\frac{1}{2}$; thus the spins of such a band would be $I=\frac{11}{2}$, $\frac{15}{2}$, $\frac{19}{2}$, ... In the prolate structure, only the levels with the same signature would be perturbed. This provides the motivation for the choice of spins for the perturbed band to be those of negative signature, $\alpha=-\frac{1}{2}$.

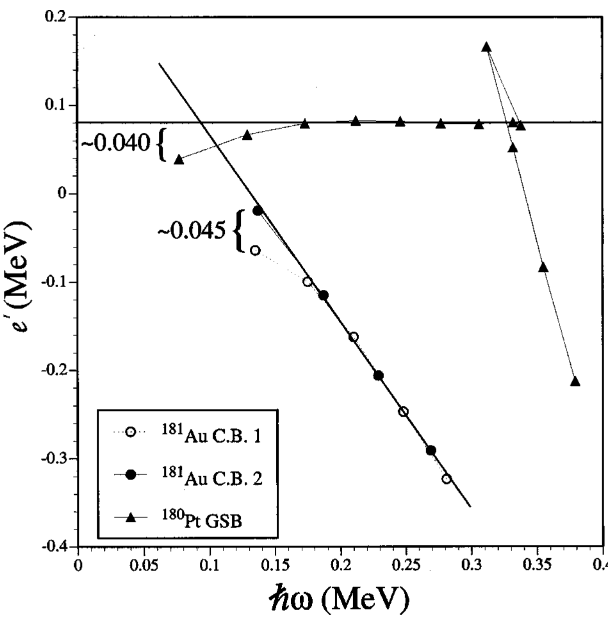

FIG. 11. Experimental quasiparticle Routhian energy of ^{180}Pt compared with the quasiparticle Routhian of the coupled band in ^{181}Au. The Harris reference parameters are $\mathcal{J}_0=27.47\hbar^2$/MeV and $\mathcal{J}_1=179.2\hbar^4$/MeV^3.

VI. DISCUSSION

There are two features of interest in the systematic analysis of the high-spin level structure of the ^{181}Au, ^{183}Au, and neighboring nuclei. The first feature of interest is the trend of the $\pi i_{13/2}$ intruder band as nuclei approach and pass through the neutron midshell $(N\sim104)$. The second point is the somewhat rare observation of decoupled bands that can be interpreted as pseudospin doublets (the $\pi h_{9/2}$ and $\pi f_{7/2}$ bands). These two features will be addressed in turn in the following sections.

A. Alignment and bandhead properties in the $\pi i_{13/2}$ intruder band

In this section, discussion will focus on two particular properties of the $\pi i_{13/2}$ intruder band: alignment effects and bandhead energy systematics. By studying these systematics of the intruder bands in odd-A Au isotopes, one can gain additional insight into deformation properties and quasiparticle excitations within these nuclei. The alignment properties of observed $\pi h_{9/2}$ $\alpha=+\frac{1}{2}$ bands are also included in this discussion as a reference.

1. Alignment and moment of inertia of intruder bands

The quasiparticle alignment characteristics of the $\pi h_{9/2}$ and $\pi i_{13/2}$ bands in the neutron deficient Au region are somewhat unusual and have been a subject of much debate over the years (see, e.g., Refs. [2,3,27–29]). In particular, the debate has centered around whether alignment properties observed in rotational bands in Ir, Pt, and Au around $N\sim108$

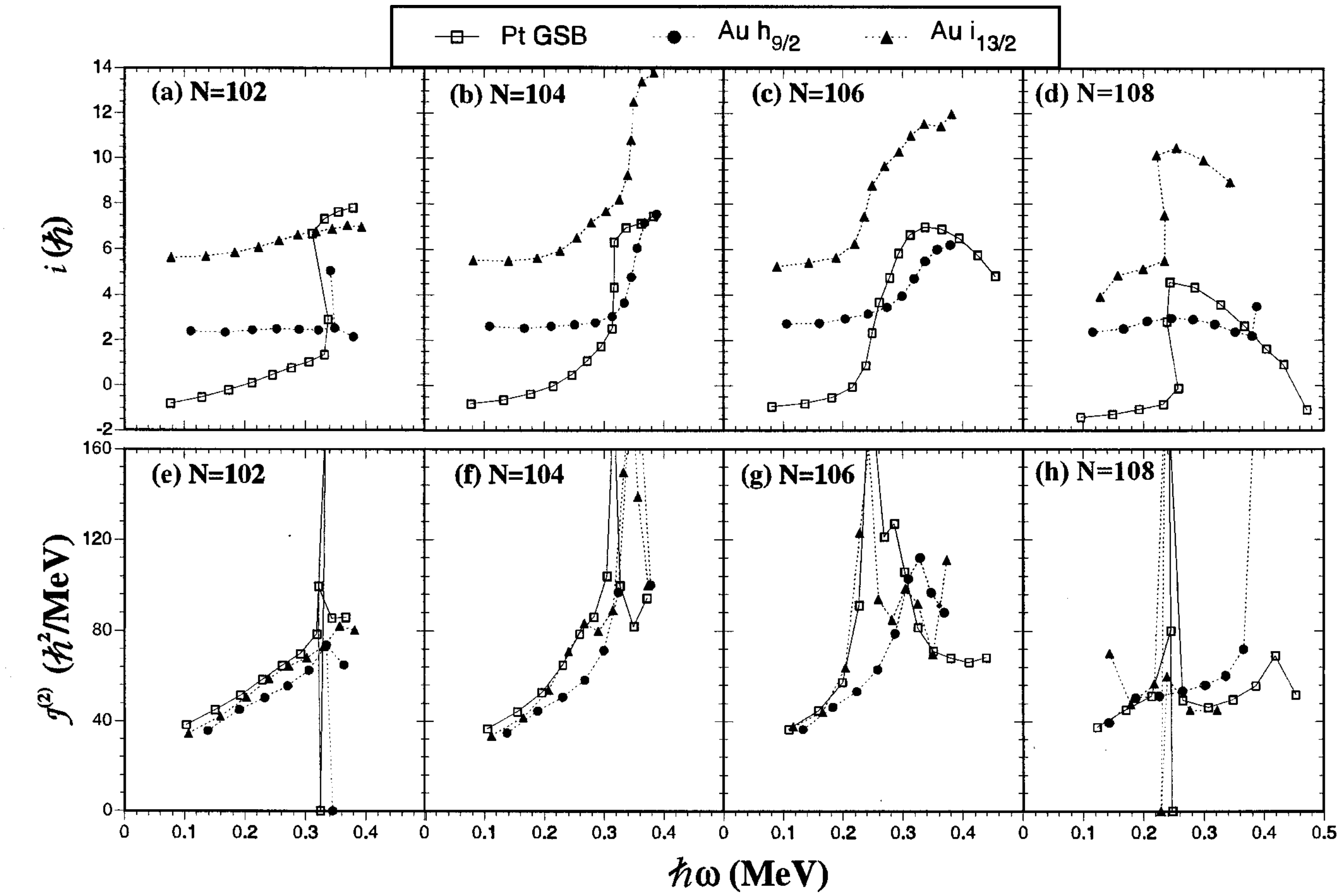

FIG. 12. Panels (a)–(d): experimental quasiparticle alignment (i) for $\pi h_{9/2}$ and $\pi i_{13/2}$ rotational bands in Au for $102 \leq N \leq 108$ and ground-state bands (GSB) in Pt. The Harris parameters are chosen to be $\mathcal{J}_0 = 29.4\hbar^2$/MeV and $\mathcal{J}_0 = 121\hbar^4$/MeV^3 such that the $\pi h_{9/2}$ band in ^{181}Au is approximately constant at low frequency. Panels (e)–(h): experimental dynamic moment of inertia ($\mathcal{J}^{(2)}$) for ground-state rotational bands (GSB) in Pt and $\pi h_{9/2}$ and $\pi i_{13/2}$ bands in Au for $102 \leq N \leq 108$. The data for Pt isotopes (in order of increasing N) come from Refs. [17,4,33,40], and ^{185,187}Au from Refs. [2,3].

are the result of a $(\pi h_{9/2})^2$ band crossing in addition to the normal $(\nu i_{13/2})^2$ crossing or that some other process is occurring. The addition of ^{181}Au and ^{183}Au to the pool of data allows one to study the evolution of alignment with changing neutron number. Illustrated in Fig. 12 are the quasiparticle alignments (i) and dynamic moments of inertia ($\mathcal{J}^{(2)}$) for the observed $\pi h_{9/2}$ and $\pi i_{13/2}$ bands in even-N Au nuclei from ^{181}Au to ^{187}Au. Also included in this figure are i and $\mathcal{J}^{(2)}$ for ground-state rotational bands in corresponding Pt nuclei. The dynamic moment of inertia is calculated using the definition in Bohr and Mottelson [30] (Sec. 4.3):

$$\mathcal{J}^{(2)} = \frac{dI_x}{d\omega}, \tag{6.1}$$

where I_x and ω are defined in Sec. V. This definition is chosen because the moment of inertia contributed by an unpaired particle is not present (i.e., $di/d\omega \approx 0$).

Excluding the $\sim 6\hbar$ of alignment contributed by the odd proton in the $\pi i_{13/2}$ band Au, one can see by examining the trend in alignment [Figs. 12(a)–12(d)] that there is a remarkable similarity between the $\pi i_{13/2}$ bands in Au compared to the Pt core band. This is particularly true for ^{187}Au [Fig. 12(d), $N = 108$] compared to ^{186}Pt. The similarities are that the slope of $\pi i_{13/2}$ alignment in Au is very similar to that of Pt, and the interaction strength and alignment gain through the band-crossing region are comparable. For emphasis of this observation, the dynamic moments of inertia for these bands are plotted in Figs. 12(e)–12(h). Excluding the points in the crossing region, one sees that the moment of inertia at a given rotational frequency ($\hbar\omega$) is nearly identical for the Au $\pi i_{13/2}$ band and the Pt ground-state band. The greatest difference occurs between the bands in ^{181}Au and ^{180}Pt($N = 102$), where $\mathcal{J}^{(2)}$ at a given frequency ($\hbar\omega$) for the $\pi i_{13/2}$ band is consistently lower than that of the Pt band.

One of the known properties of intruder bands is that the deformation of the nucleus is enhanced when the intruder orbital is occupied. Naturally, an increase in deformation should also result in an increase in the moment of inertia. The data presented in Figs. 12(e)–12(h), however, appear to contradict this in that the moments of inertia are nearly identical. It should be noted, however, as discussed in Ref. [25], that when the Fermi level is near or within the intruder shell the core is no longer significantly affected by the orbital. Nevertheless, total Routhian surface calculations [23] still predict that the deformation of $\pi i_{13/2}$ intruder bands in Au should be $\sim 5-15\%$ greater than the Pt core. For example, the predicted quadrupole deformation for the $\pi i_{13/2}$ band in ^{181}Au at a rotational frequency of $\hbar\omega = 0.171$ MeV is $\beta_2 = 0.284$, while for the ground-state band in ^{180}Pt the value is

TABLE III. Moment of inertia parameters for bands in ^{181}Au and the ground-state band in ^{180}Pt, obtained using Eq. (6.3).

Nucleus	Configuration	$i(\hbar)$	$\mathcal{J}_0(\hbar^2/\mathrm{MeV})$	$\mathcal{J}_1(\hbar^4/\mathrm{MeV}^3)$
^{181}Au	$\pi h_{9/2}\,(\alpha=+\frac{1}{2})$	2.45 ± 0.24	29.4 ± 2.3	121 ± 15
	$\pi h_{9/2}\,(\alpha=-\frac{1}{2})$	1.88 ± 0.50	26.2 ± 3.0	140 ± 12
	$\pi f_{7/2}\,(\alpha=-\frac{1}{2})$	1.25 ± 0.50	37.0 ± 3.0	132 ± 15
	$\pi i_{13/2}$	5.43 ± 0.27	31.6 ± 2.7	136 ± 18
^{180}Pt	0 q.p.	$\equiv 0$	27.5 ± 2.6	180 ± 17

$\beta_2=0.261$. This corresponds to a $\approx 9\%$ increase in deformation by occupation of the intruder orbital.

The fact that $\mathcal{J}^{(2)}$ for the supposedly more deformed ^{181}Au$\pi i_{13/2}$ band is less than the ^{180}Pt band can be understood by considering the moment of inertia at zero rotational frequency. This has been done by using an expansion of the moment of inertia to fit a plot of the *kinematic* moment of inertia ($\mathcal{J}^{(1)}$) of a particular rotational band. The kinematic moment of inertia of a rotational band can be calculated as

$$\mathcal{J}^{(1)}=\frac{I_x}{\hbar\omega}. \tag{6.2}$$

Extending the development by Harris [13], the moment of inertia of a nuclear rotational band can here be presented as

$$\mathcal{J}^{(1)}=\frac{i}{\omega}+\mathcal{J}_0+\mathcal{J}_1\omega^2, \tag{6.3}$$

where i is the quasiparticle alignment of a state, and $\mathcal{J}_0$ and $\mathcal{J}_1$ represent the static and frequency-dependent terms of the moment of inertia expansion. Note that the kinematic moment of inertia is used, because this representation of the moment of inertia is less sensitive to subtle alignment changes than the dynamic representation. The results of this fit for four bands in ^{181}Au and the ground-state band in ^{180}Pt are listed in Table III.[5] One can see from the results of this fit that the zero-frequency moment of inertia ($\mathcal{J}_0$) of the $\pi i_{13/2}$ band in ^{181}Au is $\approx 15\%$ greater than that of the ground-state band in ^{180}Pt but with a large uncertainty. To interpret this properly, one must consider the dependence of the moment of inertia on deformation. It should be noted that $\mathcal{J}_0$ not only depends on nuclear deformation but also on the pair gap energy. From the work of Belyaev [31] and Migdal [32], it can be shown that the static moment of inertia ($\mathcal{J}_0$) of nuclei with $0.2<\beta_2<0.4$ is approximately proportional to a linear function of $\sqrt{A}(\beta_2/\Delta)$, where A is the atomic number and Δ is the total pair gap energy.[6] Thus, if one considers that the $\pi i_{13/2}$ orbital in Au is far enough from the Fermi surface so that blocking this orbital does not significantly reduce the pairing energy, the difference of the $\mathcal{J}_0$ value in the $\pi i_{13/2}$ band in ^{181}Au compared to the ground-state band in ^{180}Pt is indicative that that deformation of ^{181}Au when the $\pi i_{13/2}$ band is occupied is measurably larger than ^{180}Pt. The large uncertainty of the $\mathcal{J}_0$ extraction, however, makes this comparison qualitative at best.

An alternative method to infer the relative deformation of a nucleus is the $(\nu i_{13/2})^2$ crossing frequency ($\hbar\omega_c$). It has been demonstrated (e.g., Jin *et al.* [25]) that a larger relative deformation delays the frequency at which the $\nu i_{13/2}$ alignment occurs. A difficulty arises when extracting the crossing frequency of particular bands, however, because of the unusual alignment patterns observed in $N=104-108$. For example, the very low frequency crossing observed in ^{187}Au and ^{186}Pt has been interpreted as arising from a weak interaction $(\pi h_{9/2})^2$ alignment [3,28,29]. The nonobservation of a $(\nu i_{13/2})^2$ crossing in these nuclei is the result of a delay caused by the occurrence of a deformed shell gap at $N=108$. In addition, the alignment patterns in ^{185}Au and ^{184}Pt suggest that both $(\pi h_{9/2})^2$ and $(\nu i_{13/2})^2$ crossings occur at similar frequencies, and has been interpreted as such in Refs. [2,33]. In this interpretation, the interaction strength increases for the $(\pi h_{9/2})^2$ crossing in $N=106$ nuclei compared to $N=108$, thus the reason an upbend occurs in the $N=106$ nuclei rather than a backbend. The $(\nu i_{13/2})^2$ crossing is observed because the gap at $N=108$ has less influence and does not significantly delay the $(\nu i_{13/2})^2$ alignment.

For ^{182}Pt [see Fig. 12(b)], the alignment has a smoothly increasing slope as a function of $\hbar\omega$, but then undergoes a sharp crossing at about $\hbar\omega=0.32$ MeV. The pattern in the $\pi i_{13/2}$ band of ^{183}Au is similar to that in ^{182}Pt; however, there is a small bump in alignment at about $\hbar\omega=0.30$ MeV and the sharp crossing is somewhat delayed with respect to ^{182}Pt ($\hbar\omega=0.34$ MeV). Cranked-shell-model calculations presented by Jin *et al.* [25] indicate that the $(\pi h_{9/2})^2$ crossing frequency becomes increasingly delayed and the interaction strength becomes progressively larger as neutron number decreases to $N=102$, where these observables are expected to be a maximum. While the $(\nu i_{13/2})^2$ crossing frequency is also predicted to maximize at $N=102$, the interaction strength is predicted to be the weakest. Based on these results, the smoothly increasing slope observed in ^{182}Pt and in the $\pi i_{13/2}$ band in ^{183}Au is the result of the beginning of a strong interaction $(\pi h_{9/2})^2$ alignment. Before the $h_{9/2}$ protons are fully aligned, a weak interaction $(\nu i_{13/2})^2$ alignment occurs. The reason that the $(\nu i_{13/2})^2$ crossing in ^{183}Au is delayed with respect to ^{182}Pt is due to the larger deformation of the $\pi i_{13/2}$ configuration in ^{183}Au.

[5] Also included in Table III are the results of a fit to $\pi h_{9/2}$ and $\pi f_{7/2}$ bands in ^{181}Au. These results will be discussed in Sec. VI B 1.

[6] Bohr and Mottelson developed Eq. 4-128 in Ref. [30] from Belyaev's and Migdal's work. A Taylor expansion of this equation reveals this linear relationship.

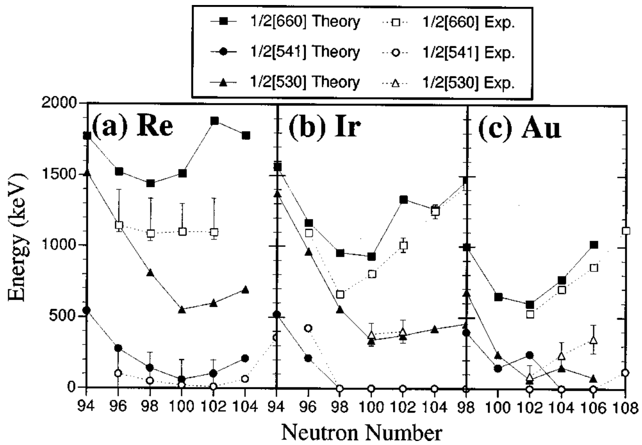

FIG. 13. Experimental and calculated bandhead energies for $\pi h_{9/2}$, $\pi f_{7/2}$, and $\pi i_{13/2}$ states in odd-*A* (a) Re, (b) Ir, and (c) Au nuclei. The data for Re istotopes (in order of increasing *N*) come from Refs. [34,41,42,16,43,44], Ir isotopes from Refs. [35,45,42,25,26,28,46], and ^{185,187}Au from Refs. [2,3].

As noted previously in this section, the alignment trends for the $\pi i_{13/2}$ band of ^{181}Au and the ground-state band of ^{180}Pt are smoothly increasing. Unlike the bands observed in ^{183}Au and ^{182}Pt, this increase is not characterized by a significant change in the slope. Analogous to the interpretation of ^{183}Au and ^{182}Pt, one possible explanation is that the increases observed in the ^{181}Au $\pi i_{13/2}$ and ^{180}Pt bands is the result of a very large interaction $(\pi h_{9/2})^2$ alignment. While such a smooth increase is certainly difficult to justify as an alignment process, support for this interpretation comes from the observation of the alignment trend in the $\pi h_{9/2}$ band [see the circles in Fig. 12(a)]. Up to $\hbar\omega \approx 0.34$ MeV, the alignment of the $\pi h_{9/2}$ band is nearly constant with frequency. This is naturally a consequence of the choice of reference; however, it is clear that the slope of the $\pi h_{9/2}$ alignment curve is less than that of the $\pi i_{13/2}$ and Pt bands. A proton occupying the $h_{9/2}$ orbital blocks the alignment process, thus a smooth increase in the $\pi h_{9/2}$ band is inhibited.

Unlike other Au nuclei, a sharp crossing is not observed in the ^{181}Au $\pi i_{13/2}$ band up to a frequency of $\hbar\omega \approx 0.4$ MeV; however, a crossing is observed at $\hbar\omega \approx 0.32$ MeV in ^{180}Pt. As is the case for the $N=104$ nuclei, the sharp crossing observed in ^{180}Pt is likely the result of a $(\nu i_{13/2})^2$ alignment. This crossing is not observed in the $\pi i_{13/2}$ ^{181}Au band, because the larger deformation of the intruder configuration delays the crossing to a frequency that is beyond the sensitivity of the experiment.

Because of the complicated alignment processes, it is difficult to use crossing frequency as a strong indicator of deformation. Nevertheless, the delay of the $(\nu i_{13/2})^2$ crossing in $\pi i_{13/2}$ bands of ^{181}Au and ^{183}Au with respect to corresponding bands in Pt provides another piece of evidence of the larger deformation of the intruder configurations.

2. Bandhead energies of intruder bands

The experimental and calculated bandhead energies for known $\pi i_{13/2}$, $\pi h_{9/2}$, and $\pi f_{7/2}$ configurations in Re ($Z=75$), Ir ($Z=77$), and Au ($Z=79$) nuclei are illustrated in Fig. 13. For cases where the bandhead is not observed, the bandhead energies are obtained from extrapolation of the rotational band with a least squares fit to a variable moment of inertia function. Appropriate uncertainties related to the extrapolation are noted in the figures. For $N=96$–102 Re isotopes the excitation energy of the $\pi h_{9/2}$ bands with respect to the respective ground states is not known; however, as reported, for example, in Ref. [34], an upper limit of ≈ 200 keV can be placed on these bandheads based on relative populations of high-spin states in the observed bands. The large uncertainties in the $\pi i_{13/2}$ bands in these same Re isotopes result from the fact that these bandheads are relative to the $\pi h_{9/2}$ states.

The calculated bandhead energies are the results from an extension of the macroscopic-microscopic shell correction model discussed in Ref. [12]. Included in Fig. 13 are the theoretical bandheads (relative to the ground state in each respective nucleus) for the $\frac{1}{2}[660]$ ($\pi i_{13/2}$), $\frac{1}{2}[541]$ ($\pi h_{9/2}$), and $\frac{1}{2}[530]$ ($\pi f_{7/2}$) Nilsson configurations. This model considered only axial deformations (i.e., no γ degree of freedom). The calculated excitation energies (δE) and deformation (β_2, β_4, and β_6) for these intruder as well as ground-state configurations are shown in Tables IV, V, and VI. It should be noted that the deformation parameters shown in these tables are for configurations at zero rotational frequency. As a consequence, they do not necessarily represent the deformation at larger rotational frequencies. Thus, for theoretical comparisons at high frequencies, such as those described in Sec. VI A 1, deformation parameters are not extracted from these tables, but rather from models where the deformation is calculated at $\hbar\omega \approx 0.2$ MeV.

There are several trends in the theoretical bandheads that can be noted. First, the energies of the intruder configurations are lowest in Au isotopes and become successively higher in energy in Ir and Re. This is simply indicative that the Fermi level in Au is much closer to the intruder states compared to the lower-*Z* nuclei. The bandheads of all three intruder configurations exhibit minima in nuclei in this region. As seen in lighter nuclei, prolate collective effects are maximum around the neutron midshell ($N=104$); thus it is expected that the energy of these prolate intruder bands would minimize in this region. One can see from Fig. 13 that the specific point of minimization for a given configuration and proton value changes. For example, the energy of the $\frac{1}{2}[660]$ configuration in Re isotopes is lowest at $N=98$, while the orbital is lowest at $N=100$ in Ir and $N=102$ in Au.

It can be seen that the values from the theoretical calculations agree with the experimental results rather well. The greatest systematic disagreement occurs in the observed bandhead of identified $\pi i_{13/2}$ configurations in Re isotopes. This disagreement, however, may not be a shortcoming of the calculation, but rather a difficulty of the experimental assignment of the $\pi i_{13/2}$ bands in Re. Bark *et al.* [16] demonstrated that, of the several low-lying positive-parity bands observed in ^{177}Re, none could be associated with a pure one-quasiparticle $\pi i_{13/2}$ configuration, but rather all are complicated mixtures of three-quasiparticle bands. Bark *et al.* also call into question the $\pi i_{13/2}$ assignments in other Re isotopes. Thus it is likely that the experimental bandhead energies shown as $\frac{1}{2}[660]$ configurations in Fig. 13(a) are, in fact, bandheads of three-quasiparticle configurations.

TABLE IV. Calculated bandhead excitation energies (δE), equilibrium deformation parameters (β_2, β_4, and β_6) for ground-state and intruder configurations in odd-A isotopes of Re.

Nucleus	$\Omega[Nn_z\Lambda]$	n_Ω	β_2	β_4	β_6	δE (keV)
^{169}Re$_{94}$	$\frac{9}{2}[514]$	1	0.176	−0.002	−0.007	0
	$\frac{1}{2}[541]$	8	0.216	0.032	0.007	541
	$\frac{1}{2}[530]$	9	0.211	0.009	−0.012	1517
	$\frac{1}{2}[660]$	10	0.235	0.055	0.015	1774
^{171}Re$_{96}$	$\frac{9}{2}[514]$	1	0.193	−0.001	−0.008	0
	$\frac{1}{2}[541]$	8	0.230	0.019	0.003	276
	$\frac{1}{2}[530]$	9	0.238	0.006	−0.016	1141
	$\frac{1}{2}[660]$	10	0.242	0.037	0.006	1523
^{173}Re$_{98}$	$\frac{9}{2}[514]$	1	0.211	−0.006	−0.010	0
	$\frac{1}{2}[541]$	8	0.243	0.009	−0.004	141
	$\frac{1}{2}[530]$	9	0.284	0.011	−0.012	810
	$\frac{1}{2}[660]$	10	0.250	0.019	0.000	1439
^{175}Re$_{100}$	$\frac{9}{2}[514]$	1	0.226	−0.013	−0.012	0
	$\frac{1}{2}[541]$	8	0.253	−0.004	−0.006	60
	$\frac{1}{2}[530]$	9	0.298	−0.002	−0.018	551
	$\frac{1}{2}[660]$	10	0.251	0.021	0.000	1512
^{177}Re$_{102}$	$\frac{5}{2}[402]$	4	0.235	−0.032	−0.008	0
	$\frac{1}{2}[541]$	8	0.260	−0.018	−0.008	102
	$\frac{1}{2}[530]$	9	0.297	−0.027	−0.011	598
	$\frac{1}{2}[660]$	10	0.236	−0.002	−0.006	1883
^{179}Re$_{104}$	$\frac{5}{2}[402]$	4	0.232	−0.046	−0.005	0
	$\frac{1}{2}[541]$	8	0.258	−0.032	−0.003	209
	$\frac{1}{2}[530]$	9	0.275	−0.040	−0.017	694
	$\frac{1}{2}[660]$	10	0.266	−0.019	−0.011	1783

In contrast to the Re isotopes, a comparison of the calculated and experimental $\pi i_{13/2}$ bandheads in Ir and Au isotopes in Figs. 13(b) and 13(c) shows remarkable agreement. The largest disagreement in the trend occurs for $N=98$ in Ir. As noted earlier, the theoretical calculations predicted that the $\pi i_{13/2}$ configuration would minimize at $N=100$ in Ir; however, the $\pi i_{13/2}$ orbital is observed to continue to decrease at $N=98$. The calculations predict that the ground state of ^{173}Ir is $\frac{11}{2}[505]$. While evidence [35] clearly indicates that the $\pi h_{9/2}$ configuration in ^{173}Ir is excited, the ground-state configuration was not clearly established experimentally. Nevertheless, the change in the ground-state configuration when going from ^{175}Ir ($N=98$) to ^{173}Ir ($N=96$) is properly predicted.

B. Alignment and deformation properties in $\pi h_{9/2}$-$\pi f_{7/2}$ bands

As the Fermi level increases into the $\pi h_{9/2}$ shell, the bandhead energy becomes low enough that the unfavored signature of this intruder band is observed. As the Fermi level increases further, evidence of the $\pi f_{7/2}$ band becomes apparent. In 1986, the first identification of a low-lying $\pi f_{7/2}$ rotational band in a nucleus below lead was reported in ^{185}Au [2]. Since that time, a $\pi f_{7/2}$ band has been identified in ^{179}Ir [25]. Two new cases are now presented for ^{183}Au and ^{181}Au in this article.

The $\pi h_{9/2}$ and $\pi f_{7/2}$ bands have a unique relationship in neutron-deficient odd-A Au and Ir compared to other observed bands in these nuclei. For example, Jin *et al.* [25] identified several rotational bands in ^{179}Ir with spectroscopic assignments $\frac{1}{2}^-[541]$, $\frac{1}{2}^-[530]$, $\frac{9}{2}^-[514]$, $\frac{5}{2}^+[402]$, and $\frac{1}{2}^+[660]$. In the latter three cases, each configuration is rather pure in that each orbital has a unique combination of K and parity. The $\pi h_{9/2}$ ($\frac{1}{2}^-[541]$) and $\pi f_{7/2}$ ($\frac{1}{2}^-[530]$) orbitals, however, are both low K and negative parity, and the classification of these bands in the basis of asymptotic quantum numbers becomes less clear since the configurations are heavily mixed. Because of this configuration mixing, enhanced correlations between these bands are observed, thus further increasing the difficulty in classifying these bands. The reason for the existence of this pair of negative-parity low-K structures is a direct result of the strong nucleonic spin-orbit coupling present in the nuclear system. Because of the spin-orbit coupling, the $h_{9/2}$ and $f_{7/2}$ single-particle spherical shell states are nearly degenerate in energy. This can be clearly seen at $\beta_2=0$ in the calculated single-particle proton level diagram (Fig. 7). As seen in this figure, the onset of quadrupole deformation does not break the near degeneracy of the related $\pi h_{9/2}$ and $\pi f_{7/2}$ orbitals, where the $(2j+1)$-fold degenerate shells are split into doubly degenerate states that are typically labeled by the asymptotic Nils-

TABLE V. Calculated bandhead excitation energies (δE), equilibrium deformation parameters (β_2, β_4, and β_6) for ground-state and intruder configurations in odd-A isotopes of Ir.

Nucleus	$\Omega[Nn_z\Lambda]$	n_Ω	β_2	β_4	β_6	δE (keV)
$^{171}Ir_{94}$	$\frac{11}{2}[505]$	1	0.140	−0.001	−0.003	0
	$\frac{1}{2}[541]$	8	0.194	0.029	0.011	519
	$\frac{1}{2}[530]$	9	0.188	0.007	−0.008	1374
	$\frac{1}{2}[660]$	10	0.232	0.062	0.015	1560
$^{173}Ir_{96}$	$\frac{11}{2}[514]$	1	0.154	−0.005	−0.004	0
	$\frac{1}{2}[541]$	8	0.208	0.020	0.006	213
	$\frac{1}{2}[530]$	9	0.241	0.031	−0.003	965
	$\frac{1}{2}[660]$	10	0.239	0.044	0.009	1166
$^{175}Ir_{98}$	$\frac{1}{2}[541]$	8	0.220	0.010	0.001	0
	$\frac{1}{2}[530]$	9	0.259	0.020	−0.009	559
	$\frac{1}{2}[660]$	10	0.244	0.031	0.003	955
$^{177}Ir_{100}$	$\frac{1}{2}[541]$	8	0.229	0.013	−0.001	0
	$\frac{1}{2}[530]$	9	0.274	0.006	−0.015	340
	$\frac{1}{2}[660]$	10	0.250	0.016	−0.002	931
$^{179}Ir_{102}$	$\frac{1}{2}[541]$	8	0.237	−0.014	−0.004	0
	$\frac{1}{2}[530]$	9	0.279	−0.009	−0.017	372
	$\frac{1}{2}[660]$	10	0.275	−0.009	−0.015	1335
$^{181}Ir_{104}$	$\frac{1}{2}[541]$	8	0.236	−0.028	0.000	0
	$\frac{1}{2}[530]$	9	0.257	−0.031	−0.012	421
	$\frac{1}{2}[660]$	10	0.257	−0.012	−0.005	1262
$^{183}Ir_{106}$	$\frac{1}{2}[541]$	8	0.233	−0.041	0.005	0
	$\frac{1}{2}[530]$	9	0.249	−0.056	−0.009	456
	$\frac{1}{2}[660]$	10	0.243	−0.031	0.003	1467

son quantum numbers: $\Omega^\pi[Nn_z\Lambda]$. For example, $\frac{1}{2}^-[541]$ and $\frac{1}{2}^-[530]$ in Fig. 7 are seen to be nearly degenerate even up to the highest deformation.

One would expect that rotational bands based on these orbitals would be quite similar since the configurations are so mixed. On the contrary, rotational bands from these configurations exhibit different properties and interact in a manner that is not readily understood. Discussion of the details of these differences follows in the sections below. Specific properties to be addressed are the alignment trends and branching ratios of the $\pi h_{9/2}$-$\pi f_{7/2}$ bands, as well as the observed interactions of these rotational structures. The properties are analyzed in the framework of cranking and particle-rotor models. An example where mixed configurations of strongly coupled bands are observed are the $\frac{5}{2}^+[402]$ and $\frac{7}{2}^+[404]$ rotational bands in ^{175}Re [36].

1. Quasiparticle Routhian energy and alignment

Figure 14 shows the experimental Routhian energies and alignments for nuclei where $\alpha=-\frac{1}{2}$ $\pi h_{9/2}$ and $\pi f_{7/2}$ bands have been reported. Panels (1a)–(4a) indicate cranked-shell model Routhian energies for negative-parity bands in these nuclei. The calculation is a pairing self-consistent cranking model [37], where the particle-hole mean field is approximated by an ω-independent Woods-Saxon potential. The deformations used in each nucleus were extracted from the lowest $(\pi,\alpha)=(-,+\frac{1}{2})$ configuration from total Routhian surface calculations [23]. These parameters (β_2, β_4, and γ) for the four nuclei are listed in Table VII. The labeling for the theoretical bands is consistent with Ref. [2], i.e., ‘‘a’’ labels the lowest $\alpha=-\frac{1}{2}$ band, ‘‘b’’ the lowest $\alpha=+\frac{1}{2}$ band, and ‘‘c’’ the second lowest $\alpha=-\frac{1}{2}$ band. The doubly degenerate band related to the strongly coupled $\pi h_{11/2}$ orbital is labeled in each panel.

From the comparison of the theoretical Routhian energies with the experimental values, it is clear that the two $\pi h_{9/2}$ signature partners (the squares and circles) can be associated with the ‘‘b’’ and ‘‘a’’ configurations, respectively, in the calculations. Not only is the converging trend of the two signatures toward lower frequency reproduced, but there is good qualitative agreement of the energy splitting between the bands. Of course, the calculations are made assuming that the quasiparticle mean field is the same for all configurations; thus such a direct comparison of states is only appropriate when deformation parameters and pairing fields are similar. The good agreement of configurations ‘‘b’’ and ‘‘a’’ with the experimental values clearly demonstrates the similar deformation and pairing field between the two signatures. The comparison of ‘‘c’’ with the experimental $\pi f_{7/2}$ band is an example where the approximation of a similar mean field does not appear to be valid. In the calculation, the ‘‘a’’ and ‘‘c’’ configurations are nearly parallel to one another as a

TABLE VI. Calculated bandhead excitation energies (δE) and equilibrium deformation parameters (β_2, β_4, and β_6) for ground-state and intruder configurations in odd-A isotopes of Au.

Nucleus	$\Omega[Nn_z\Lambda]$	n_Ω	β_2	β_4	β_6	δE (keV)
^{177}Au$_{98}$	$\frac{3}{2}[402]$	6	0.117	−0.008	−0.001	0
	$\frac{1}{2}[541]$	8	0.195	0.018	0.002	396
	$\frac{1}{2}[530]$	9	0.251	0.028	−0.005	680
	$\frac{1}{2}[660]$	10	0.244	0.026	−0.001	998
^{179}Au$_{100}$	$\frac{3}{2}[402]$	6	0.130	−0.013	0.000	0
	$\frac{1}{2}[541]$	8	0.215	0.004	−0.006	146
	$\frac{1}{2}[530]$	9	0.266	0.017	−0.011	240
	$\frac{1}{2}[660]$	10	0.246	0.020	0.002	649
^{181}Au$_{102}$	$\frac{11}{2}[505]$	1	0.165	−0.016	0.004	0
	$\frac{3}{2}[532]$	6	0.263	−0.002	−0.013	4
	$\frac{1}{2}[530]$	9	0.269	−0.002	−0.015	65
	$\frac{1}{2}[541]$	8	0.263	−0.004	−0.014	240
	$\frac{1}{2}[660]$	10	0.251	0.008	−0.004	596
^{183}Au$_{104}$	$\frac{1}{2}[541]$	8	0.226	−0.022	−0.003	0
	$\frac{1}{2}[530]$	9	0.261	−0.019	−0.009	151
	$\frac{1}{2}[660]$	10	0.254	−0.004	−0.006	769
^{185}Au$_{106}$	$\frac{1}{2}[541]$	8	0.223	−0.038	−0.001	0
	$\frac{1}{2}[530]$	9	0.148	−0.033	0.003	79
	$\frac{1}{2}[660]$	10	0.250	−0.020	0.004	1022

function of $\hbar\omega$, which is clearly not the case in experimental observation. Larabee *et al.* [2] attributed the gradually increasing alignment in the $\pi f_{7/2}$ band of ^{185}Au to breaking of a pair of $h_{9/2}$ protons.

The origin of this interpretation was discussed in Sec. VI A 1. If the increasing alignment observed in $\pi f_{7/2}$ bands is to be interpreted as a result of a $\pi h_{9/2}$ crossing, then it would be expected that the backbending features of the $\pi i_{13/2}$ band would be at least qualitatively reproduced by the $\pi f_{7/2}$ bands. As can be seen in Figs. 14(1c)–14(4c), the $\pi f_{7/2}$ bands in all these nuclei have a gradually increasing alignment at least partially consistent with $\pi i_{13/2}$ systematics. Just these data alone, however, are insufficient to conclusively state that the rise in alignment of $\pi f_{7/2}$ is the result of a ($\pi h_{9/2}$) crossing.

An alternative interpretation is to consider that the difference in the alignments is related to shape changes. Since lifetime data[7] are not available for these levels, alternative methods must be chosen in order to infer relative deformations. A parameter for which a relationship with deformation is clearly evident is the moment of inertia.[8] Thus, a comparison of the extracted $\mathcal{J}_0$ values of respective rotational bands can be related to the relative deformation difference (provided noncollective excitations do not play a significant role).

As a representative example, the i, $\mathcal{J}_0$, and $\mathcal{J}_1$ parameters were extracted from a fit of the moments of inertia for the three bands in ^{181}Au. The results of this fit are listed in Table III. To within the uncertainties of the extraction from $\mathcal{J}^{(1)}$, the $\mathcal{J}_0$ values for the $\pi h_{9/2}$ signature partners are approximately the same, but the $\pi f_{7/2}$ band has $\mathcal{J}_0$ that is clearly much larger than both $\pi h_{9/2}$ values. If one assumes $\mathcal{J}_0 \propto \beta_2/\Delta$ and the pair gap energy for the three bands is the same, the deformation for the $\pi f_{7/2}$ band is $\approx$25% greater than that of the $\pi h_{9/2}$ configuration. While not as great as suggested by the $\mathcal{J}^{(1)}$ analysis, a large increase in deformation is predicted in bandhead calculations for the $\pi f_{7/2}$ orbital compared to the $\pi h_{9/2}$ configuration (see Table VI); however, these calculations are not necessarily indicative of deformations at non-zero rotational frequencies.

While it is difficult theoretically to confirm the deformation difference suggested from the $\mathcal{J}_0$ analysis, there is at least one other observable that contradicts the deformation increase. That is the frequency at which $\nu i_{13/2}$ alignment occurs ($\hbar\omega_c$), as discussed in Sec. VI A 1. The $\nu i_{13/2}$ alignment is observed as a backbend in the $\pi f_{7/2}$ band (triangles) in Fig. 14(2c). The beginning of the $\nu i_{13/2}$ alignment is also observed in the $\pi h_{9/2}$ band (squares) in the same figure. In the case of ^{181}Au, the backbend in the $\pi f_{7/2}$ band occurs earlier ($\hbar\omega_c$=0.30 MeV) than for the favored $\pi h_{9/2}$ band ($\hbar\omega_c$=0.35 MeV), implying that the $\pi f_{7/2}$ band is less deformed than the $\pi h_{9/2}$ band.

In summary, the pattern that the alignment of the $\pi f_{7/2}$ band smoothly increases with respect to the $\pi h_{9/2}$ alignment is consistent for all observed cases. This effect, however, cannot be easily interpreted as a strongly interacting $\pi h_{9/2}$

[7]From level lifetimes, one can obtain $B(E2)$ transition rates from which the charge quadrupole moment and deformation can be determined in a model-dependent fashion.

[8]This relationship was discussed in Sec. VI A 2.

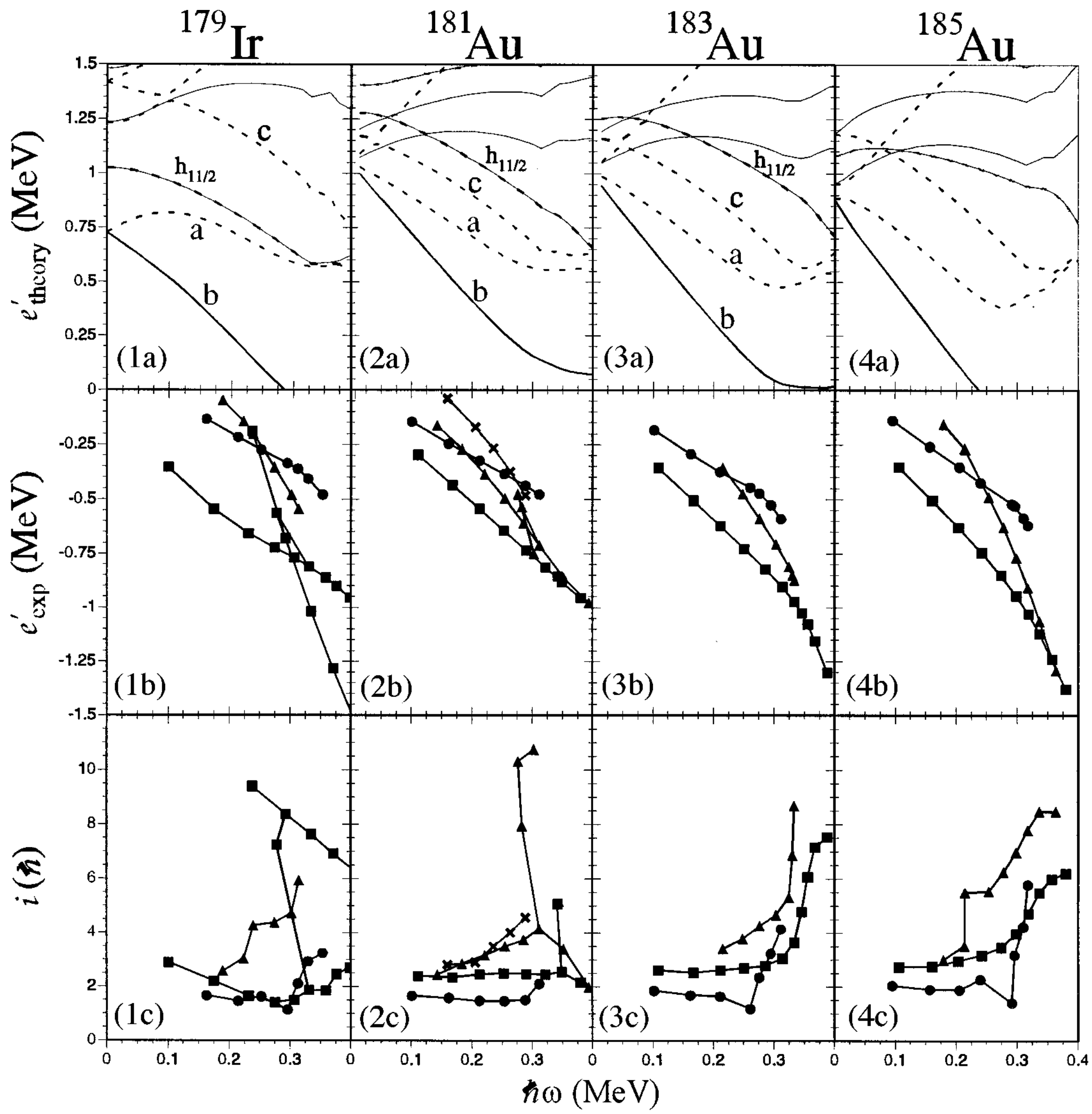

FIG. 14. Routhian and alignment plots of $\pi h_{9/2}$ and $\pi f_{7/2}$ bands for ^{179}Ir, ^{181}Au, ^{183}Au, and ^{185}Au. The figures labeled (1a)–(4a) are Routhians for negative-parity states resulting from a cranked-shell model calculation. The solid and dashed lines in (a) panels indicate states with $\alpha=+\frac{1}{2}$ and $-\frac{1}{2}$, respectively. Details of the calculation are provided in the text. Panels (b) and (c) show experimental Routhians and alignments with Harris parameters $\mathcal{J}_0=29.8\ \hbar^2$/MeV and $\mathcal{J}_1=132.1\ \hbar^4$/MeV^2. The square symbols represent the $\alpha=+\frac{1}{2}\ \pi h_{9/2}$ bands, the circles $\alpha=-\frac{1}{2}\pi h_{9/2}$, and the triangles $\alpha=-\frac{1}{2}\pi f_{7/2}$. The crosses in (2b) and (2c) denote band 4 from ^{181}Au.

crossing. With the two conflicting interpretations of the deformation, it is difficult to explain the alignment increase as a result of a deformation difference between the $\pi h_{9/2}$ and $\pi f_{7/2}$ bands. The reason for this increase in alignment remains an unresolved issue.

TABLE VII. Deformation parameters obtained from total Routhian surface calculations [23] for the lowest $(\pi,\alpha)=(-,+\frac{1}{2})$ configuration for the individual nuclei.

Nucleus	β_2	β_4	$\gamma(°)$
^{185}Au	0.227	−0.028	6.9
^{183}Au	0.235	−0.017	4.0
^{181}Au	0.237	−0.005	2.7
^{179}Ir	0.233	−0.013	3.1

2. B(M1)/B(E2) branching ratio

In the previous section, the identification of the various decoupled negative-parity bands was discussed. There are a number of $\Delta I=1$ transitions observed decaying from both the unfavored $\pi h_{9/2}$ and the $\pi f_{7/2}$ band into the favored $\pi h_{9/2}$ band. To facilitate the discussion, we refer to transitions from the $\pi f_{7/2}$ to the favored $\pi h_{9/2}$ band as interband transitions and unfavored $\pi h_{9/2}$ to favored $\pi h_{9/2}$ as intraband transitions. In this section, the $B(M1;I\to I-1)/B(E2;I\to I-2)$ reduced transition ratios [referred to henceforth as $B(M1)/B(E2)$] for these transitions in ^{179}Ir, ^{181}Au, and ^{183}Au are extracted from the data and compared to theoretical models. The experimental and theoretical $B(M1)/B(E2)$ ratios are illustrated in Fig. 15. Also included in this figure are the branching ratios for $\pi h_{11/2}$ bands observed in ^{179}Ir and ^{181}Au. The $B(M1)/B(E2)$ values are calculated from the experimental data using Eq. (5.1).

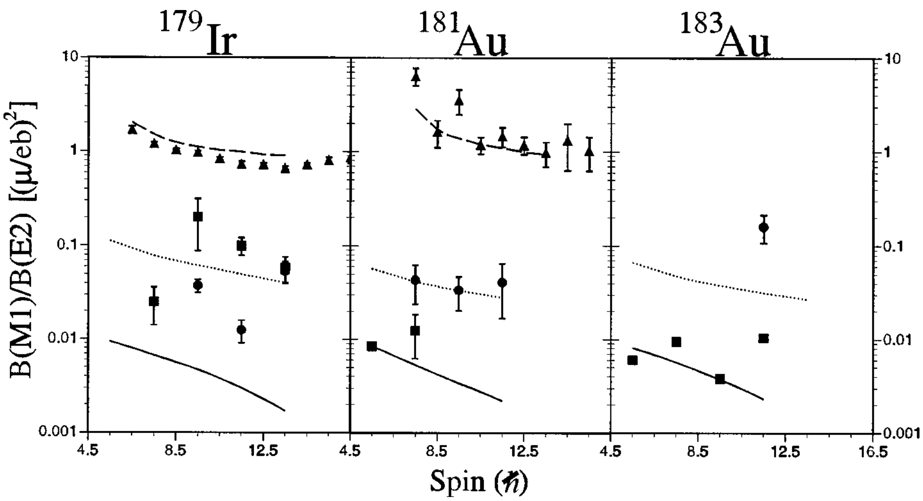

FIG. 15. Experimental $B(M1)/B(E2)$ compared with calculations for ^{179}Ir, ^{181}Au, and ^{183}Au. The squares correspond to $B(M1)/B(E2)$ values for transitions within the $\pi h_{9/2}$ bands. Circles correspond to $\pi f_{7/2} \rightarrow \pi h_{9/2}$ transitions, and triangles $\pi h_{11/2}$ intraband transitions. The solid, dotted, and dashed lines indicate the results from particle-rotor calculations for the $\pi h_{9/2}$, $\pi f_{7/2}$, and $\pi h_{11/2}$ bands, respectively. Details of the calculation are presented in the text.

The mixing ratio is not known for most transitions presented in Fig. 15 and, for those bands where the mixing ratio is known, the effect on the $B(M1)/B(E2)$ ratio is less than 10%. Since this effect is less than the uncertainty in most values, and to maintain consistency where the ratios are not known, δ was assumed to be zero in Eq. (5.1).

A comparison of the experimental transition ratios of the interband and intraband γ rays indicates that the interband rates are larger than the intraband values in ^{181}Au and ^{183}Au. These transition rates are reversed in ^{179}Ir. The expectation is that transition matrix elements between signature partners would be the largest since the wave functions of these bands essentially differ by only a rotation. Interband transitions would occur as a result of configuration mixing, but these rates are in general smaller than for intraband transitions. It is clear that the wave functions of the $\pi f_{7/2}$ and $\pi h_{9/2}$ bands are very mixed and thus strong interband transitions are likely, but it is unexpected that these interband transitions are stronger than the intraband transitions. Theoretical calculations were performed for these bands so that this problem could be better understood.

A particle-rotor model with a Woods-Saxon potential is used in the calculation of the theoretical $B(M1)/B(E2)$ ratios. The deformation of the core was chosen from the TRS predictions for the lowest $(\pi,\alpha)=(-,+\frac{1}{2})$ configuration for the individual nuclei. These are the same parameters chosen for the cranked-shell model calculations in Sec. VI B 1 with the exception that γ was set to zero for all three nuclei. Since γ was predicted to be less than 5° for all three, this is a reasonable assumption. In this model, the value $E(2_1^+)$, the excitation energy of the first 2^+ level in the effective core, is required for parametrizing the effective core. To estimate this parameter, we use the Grodzins formula

$$E(2_1^+)=\frac{1225}{\beta_2 A^{7/3}}. \quad (6.4)$$

For ^{179}Ir and ^{181}Au, the deformations of the $\pi h_{9/2}$ bands were used for the core to calculate the matrix elements of $\pi h_{11/2}$ bands. From the output of the model calculations, a clear identification of a $\pi f_{7/2}$ and $\alpha=-\frac{1}{2}\pi h_{9/2}$ band could not be established, because the two configurations are so mixed. For purposes of comparison, the lower energy levels of a given spin are defined as the unfavored $\pi h_{9/2}$ band and conversely the higher levels the $\pi f_{7/2}$ band. The results of these calculations for the $\pi h_{9/2}$ and $\pi f_{7/2}$ band are denoted as solid and dotted lines, respectively, in Fig. 15. The results for the $\pi h_{11/2}$ bands are shown as dashed lines.

In the case of ^{181}Au, the $B(M1)/B(E2)$ ratios are reproduced very well, showing that it is logical for the interband transitions to be stronger than the intraband. The ratios are also reproduced at least qualitatively for ^{183}Au. For ^{179}Ir, these values are less well predicted. While it is possible to make some comparisons of the calculations to the experimental data, a detailed analysis is difficult. The very different alignment between the $\pi f_{7/2}$ and $\pi h_{9/2}$ bands, for example, is not reproduced. In addition for this calculation, the moment of inertia of the core was dictated by the hydrodynamic relation, $\mathcal{J}\sim\beta_2^2$, and was assumed to be constant. It is thus not expected that the levels within a rotational band are well reproduced. As a consequence, the predicted level schemes for ^{179}Ir and ^{183,181}Au poorly reproduce the observed energy levels. Nevertheless, the $B(M1)/B(E2)$ ratios resulting from these calculations indicate that, due to the large amount of configuration mixing, transition rates for both interband and intraband γ rays are of the magnitude observed in experiment.

3. Interaction between $\alpha=-\frac{1}{2}$ bands

As indicated previously, the two negative-signature bands of the $\pi h_{9/2}$-$\pi f_{7/2}$ system are seen to interact in all four of the nuclei presented here. In some cases, the energy levels for the particular bands are highly perturbed by the interaction, e.g., ^{185}Au, while for other nuclei the levels are negligibly perturbed, e.g., ^{181}Au. It was recently reported by Reviol *et al.* [38] that the magnitude of the level perturbation is proportional to the interaction strength and the levels of a rotational band can be transformed by the formula

$$\Delta^4 E=\frac{1}{16}[E_\gamma(I+4)-4E_\gamma(I+2)+6E_\gamma(I)-4E_\gamma(I-2)+E_\gamma(I-4)]. \quad (6.5)$$

Figure 16 shows the $\mathcal{J}^{(2)}$ and $\Delta^4 E$ values for the negative-signature bands in ^{179}Ir, ^{181}Au, ^{183}Au, and ^{185}Au. The dy-

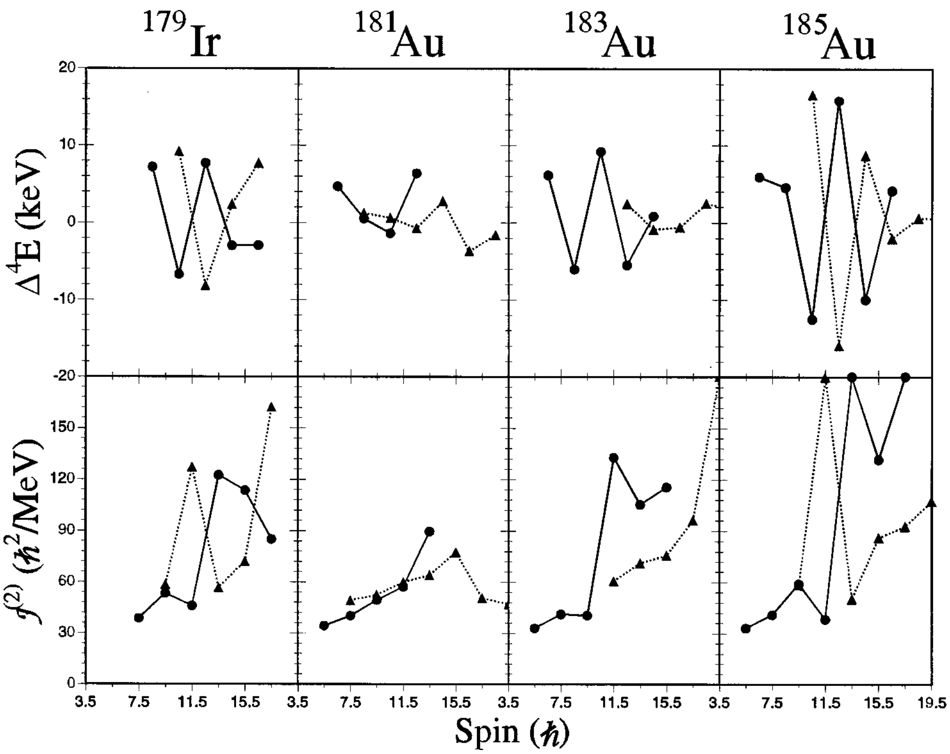

FIG. 16. $\mathcal{J}^{(2)}$ and Δ^4E vs spin (I) for $\alpha=-\frac{1}{2}$ $\pi h_{9/2}$-$\pi f_{7/2}$ bands in ^{179}Ir, ^{181}Au, ^{183}Au, and ^{185}Au. The circles represent the $\pi h_{9/2}$ band and the triangles correspond to $\pi f_{7/2}$. The lower panels indicate the $\mathcal{J}^{(2)}$ calculated from observed bands using Eq. (6.1), and the upper panels represent Δ^4E staggering extracted from experimental levels using Eq. (6.5).

namic moment of inertia, $\mathcal{J}^{(2)}$, is very sensitive to perturbations in the energy levels of rotational bands, and this can be readily observed in Fig. 16 by the large fluctuations in the moment of inertia of the bands. Because of the gradually increasing nature of $\mathcal{J}^{(2)}$, however, it is difficult to quantify a relative stagger between the different nuclei. The quantity Δ^4E is essentially a fourth-order derivative of the given rotational band; thus the gradually rising feature of $\mathcal{J}^{(2)}$ is averaged out, and a staggering related to the level perturbations is all that remains. As is illustrated in Fig. 16, the interaction between the $\pi h_{9/2}$ and $\pi f_{7/2}$ bands is largest in ^{185}Au where the staggering is as great as 16 keV. For ^{179}Ir and ^{183}Au, the interaction is about 60% that of ^{185}Au. In ^{181}Au, the staggering is essentially zero at the point where the two bands cross (levels $\frac{15}{2}$ and $\frac{19}{2}$). This indicates that there is only a very small interaction between the close-lying $\pi h_{9/2}$ and $\pi f_{7/2}$ bands in ^{181}Au.

The reason for this weak interaction in ^{181}Au may be related to the point where the $\pi h_{9/2}$ and $\pi f_{7/2}$ bands cross. The unfavored $\pi h_{9/2}$ and $\pi f_{7/2}$ bands cross at about spin $\frac{19}{2}^-$. This compares with a crossing at about $\frac{23}{2}^-$ to $\frac{27}{2}^-$ in the other nuclei. This can be seen in Routhian space as well. The rotational frequency at which the two bands cross can be determined from Figs. 14(2b), 14(3b), and 14(4b) for ^{181}Au, ^{183}Au, and ^{185}Au to be 0.20, 0.21, and 0.22 MeV, respectively. Thus, for progressively higher rotational frequencies, the interaction strength increases. As with the other aspects of the $\pi h_{9/2}$-$\pi f_{7/2}$ system, this is a feature that is not fully understood, and cannot be reproduced by the present models.

VII. CONCLUSIONS

Excited rotational states in ^{181,183}Au have been observed for the first time and have allowed the study of prolate deformations in Au nuclei across the neutron midshell ($N=104$). Four rotational bands have been established in ^{183}Au. These bands are all identified as being based upon the intruder configurations $\pi h_{9/2}$ (two signatures), $\pi f_{7/2}$, and $\pi i_{13/2}$. Bands based on these four configurations have also been seen in ^{181}Au; however, four additional structures have been discovered in this nucleus. One band (band 6 in Fig. 4) has been identified as a three-quasiparticle structure based on a $\pi i_{13/2}\otimes\nu f_{5/2}\otimes\nu f_{7/2}$ configuration. At the highest excitation energies observed ($E_x>\sim4000$ keV), this three-quasiparticle band is the most intense, and this is due to the fact that it is the yrast configuration at $I=\frac{53}{2}$.

A signature partner to this band has not been observed, but indications of its existence are seen as perturbations to the levels in band 7 of Fig. 4. A strongly coupled band in ^{181}Au is identified as a prolate $\pi h_{11/2}$ structure; however, perturbations at the bottom of this band clearly indicate mixing with an unobserved oblate $\pi h_{11/2}$ structure that is also expected to be rather low in energy in this region. A definite assignment could not be made for the weakly populated band 4; however, a possible configuration is the unfavored signature of the $\pi f_{7/2}$ band.

The alignment and moment-of-inertia properties of the $\pi i_{13/2}$ bands in odd-A Au nuclei from $N=102$ to $N=108$ were compared with the favored-signature $\pi h_{9/2}$ configurations in the respective nuclei as well as the ground-state rotational bands in the correponding Pt core nuclei. From this comparison, it was seen that the alignment trends of the $\pi i_{13/2}$ structures are remarkably similar to that in Pt ground-state bands. This is in contrast to the $\pi h_{9/2}$ bands which have a much different alignment trend. This difference can be interpreted as a result of a strongly interacting $(\pi h_{9/2})^2$ band crossing. This aligning process is blocked in the $\pi h_{9/2}$ bands, but is manifested as a gradually increasing alignment in rotational structures where this configuration is not blocked.

Results from total Routhian surface calculations indicate that the occupation of the $\pi i_{13/2}$ configuration in ^{181}Au should produce a deformation enhancement of $\approx 9\%$ compared to that of ^{180}Pt. This enhancement can be demonstrated qualitatively, by comparing the moment of inertia extrapolated to zero frequency ($\mathcal{J}_0$) for the $\pi i_{13/2}$ band in ^{181}Au and the ground-state band in ^{180}Pt. From this comparison an $\approx 10\%$ larger $\mathcal{J}_0$ value is seen in ^{181}Au. The large uncertainty in $\mathcal{J}_0$ from this extraction does not make this analysis conclusive; however, a comparison of the $(\nu i_{13/2})^2$ crossing frequencies in these bands provides another indirect indication of the relative deformation. The delay of the $(\nu i_{13/2})^2$ crossing in ^{181}Au, as well as ^{183}Au, with respect to the ground-state bands in ^{180}Pt and ^{182}Pt, respectively, illustrates the deformation enhancement induced by the occupation of an intruder band.

To examine the trend of intruder states through the neutron midshell, we compared the experimental bandhead energies of the $\pi i_{13/2}$, $\pi h_{9/2}$, and $\pi f_{7/2}$ configurations in Re, Ir, and Au isotopes with calculations using a macroscopic-microscopic shell-correction model. The downsloping trend in the $\pi i_{13/2}$ bands as the neutron midshell is approached is very well reproduced in Au and Ir. The results appear less good in Re nuclei, but this is likely the result of mixing of multiquasiparticle configurations, which is not accounted for in the model.

The unique interaction properties between $\pi h_{9/2}$ and $\pi f_{7/2}$ were also studied. It is seen that the alignment trend of the $\pi f_{7/2}$ band in the three known cases in Au isotopes as well as the one Ir case shows an upsloping character compared to the two signatures of the $\pi h_{9/2}$ configuration. This trend is similar to what is seen $\pi i_{13/2}$ bands, and thus the trend can be interpreted as $(\pi h_{9/2})^2$ alignment; however, there is insufficient data to make a conclusive statement to that effect.

To better understand the quasiparticle makeup of these mixed $\pi h_{9/2}$ and $\pi f_{7/2}$ configurations, we compared the experimental $B(M1)/B(E2)$ decay ratios from the $\pi f_{7/2}$ and $\pi h_{9/2}$ $\alpha = -\frac{1}{2}$ band to the $\pi h_{9/2}$ $\alpha = +\frac{1}{2}$ states in ^{181,183}Au and ^{179}Ir with the results of particle-rotor calculations. The experimental values were reproduced by the theoretical calculations quite well for ^{181,183}Au. The $B(M1)/B(E2)$ calculations compared less well in the more difficult case of ^{179}Ir, but the qualitative agreement was still rather good. In no case, however, could the complex alignment patterns observed between these $\pi h_{9/2}$ and $\pi f_{7/2}$ bands be reproduced.

As a final illustration of the complexity of the $\pi h_{9/2}$ and $\pi f_{7/2}$ interaction, the experimental $\mathcal{J}^{(2)}$ are shown together with $\Delta^4 E$ (a quantity chosen to illustrate the perturbations of levels from a smoothly increasing $\mathcal{J}^{(2)}$) values of $\pi h_{9/2}$ $\alpha = -\frac{1}{2}$ and $\pi f_{7/2}$ bands in ^{181,183,185}Au and ^{179}Ir. From this comparison, it can be clearly seen that the interaction strength between these two rotational bands is largest for ^{185}Au where the levels are significantly perturbed from a smoothly increasing reference. This interaction strength decreases as one goes to ^{181}Au, where there is very little perturbation in the levels. The reason for this change in interaction strength is not understood, and cannot be reproduced in any of the models that were tested.

These studies of ^{183}Au and ^{181}Au have yielded much information that helps confirm existing theories and increases our understanding of intruder bands; however, as so often happens, additional unexpected results yield more questions that remain to be answered.

ACKNOWLEDGMENTS

This work at the University of Tennessee was supported by the U.S. Department of Energy through Contract No. DE-FG02-96ER40983. ORNL is managed by Lockheed Martin Energy Research Corporation for the U.S. DOE under Contract No. DE-AC05-96OR22464.

[1] K. Heyde, P. Van Isacker, M. Waroquier, J. L. Wood, and R. A. Meyer, Phys. Rep. **102**, 291 (1983).

[2] A. J. Larabee, M. P. Carpenter, L. L. Riedinger, L. H. Courtney, J. C. Waddington, V. P. Janzen, W. Nazarewicz, J.-Y. Zhang, R. Bengtsson, and G. A. Léander, Phys. Lett. **169B**, 21 (1986).

[3] J. K. Johansson, D. G. Popescu, D. D. Rajnauth, J. C. Waddington, M. P. Carpenter, L. H. Courtney, V. P. Janzen, A. J. Larabee, Z. M. Liu, and L. L. Riedinger, Phys. Rev. C **40**, 132 (1989).

[4] *Table of Isotopes*, 8th ed., edited by R. B. Firestone (Wiley, New York, 1996), Vol. 2.

[5] M. I. Macias-Marques, C. Bourgeois, P. Kilcher, B. Roussière, J. Sauvage, M. C. Abreu, and M. G. Porquet, Nucl. Phys. **A427**, 205 (1984).

[6] A. C. Kahler, L. L. Riedinger, N. R. Johnson, R. L. Robinson, E. F. Zganjar, A. Visvanathan, D. R. Zolnowski, M. B. Hughes, and T. T. Sugihara, Phys. Lett. **72B**, 443 (1978).

[7] C. Bourgeois, P. Kilcher, B. Roussiere, J. Sauvage-Letessier, and M. G. Porquet, Nucl. Phys. **A386**, 308 (1982).

[8] K. S. Krane, Nucl. Instrum. Methods **98**, 205 (1972).

[9] J. Sauvage, C. Bourgeois, P. Kilcher, F. Le Blanc, B. Roussière, M. I. Macias-Marques, F. Bragança Gil, H. G. Porquet, H. Dautet, and the ISOCELE Collaboration, Nucl. Phys. **A540**, 83 (1992).

[10] K. S. Krane, R. M. Steffen, and R. M. Wheeler, Nucl. Data Tables **11**, 351 (1973).

[11] J. L. Wood, K. Heyde, W. Nazarewicz, M. Huyse, and P. Van Duppen, Phys. Rep. **215**, 101 (1992).

[12] W. Nazarewicz, M. A. Riley, and J. D. Garrett, Nucl. Phys. **A512**, 61 (1990).

[13] S. M. Harris, Phys. Rev. **138**, B509 (1965).

[14] C. Ekström, S. Ingelman, I. Ragnarsson, L. Robertson, and G. Wannberg, Nucl. Phys. **A348**, 25 (1980).

[15] A. Bohr and B. R. Mottelson, *Nuclear Structure* (Benjamin, Reading, MA, 1969), Vol. I.

[16] R. A. Bark, G. B. Hagemann, B. Herskind, H. J. Jensen, W. Korten, J. Wrzesinski, H. Carlsson, M. Bergström, A. Brockstedt, A. Nordlund, H. Ryde, P. Bosetti, S. Leoni, F. Ingebretsen, and P. O. Tjøm, Nucl. Phys. **A591**, 265 (1995).

[17] M. J. A. De Voigt, R. Kaczarowski, H. J. Riezebos, R. F. Noorman, J. C. Bacelar, M. A. Deleplanque, R. M. Diamond, F. S. Stephens, J. Sauvage, and B. Roussière, Nucl. Phys. **A507**, 472 (1990).

[18] W. F. Mueller, H. J. Jensen, W. Reviol, L. L. Riedinger, C.-H. Yu, J.-Y. Zhang, W. Nazarewicz, and R. Wyss, Phys. Rev. C **50**, 1901 (1994).

[19] W. Reviol, M. P. Carpenter, U. Garg, R. V. F. Janssens, I. Ahmad, I. G. Bearden, Ph. Benet, P. J. Daly, M. W. Drigert, P. B. Fernandez, T. L. Khoo, E. F. Moore, S. Pilotte, and D. Ye, Nucl. Phys. **A548**, 331 (1992).

[20] W. Reviol, L. L. Riedinger, J. y. Zhang, W. F. Mueller, and B. E. Zimmerman, Phys. Rev. C **49**, R587 (1994).

[21] W. Reviol, L. L. Riedinger, J. M. Lewis, W. F. Mueller, C. R. Bingham, J.-Y. Zhang, and B. E. Zimmerman, Phys. Scr. **T56**, 167 (1995).

[22] G. J. Lane, G. D. Dracoulis, A. P. Byrne, P. M. Walker, A. M. Baxter, J. A. Sheikh, and W. Nazarewicz, Nucl. Phys. **A586**, 316 (1995).

[23] R. Wyss, W. Satuła, W. Nazarewicz, and A. Johnson, Nucl. Phys. **A511**, 324 (1990).

[24] G. D. Dracoulis, B. Fabricius, A. M. Baxter, A. P. Byrne, K. P. Lieb, and A. E. Stuchbery, Nucl. Phys. **A534**, 173 (1991).

[25] H.-Q. Jin, L. L. Riedinger, C. R. Bingham, M. P. Carpenter, V. P. Janzen, C.-H. Yu, L. Zhou, P. B. Semmes, J.-Y. Zhang, M. A. Riley, C. Baktash, M. L. Halbert, N. R. Johnson, I. Y. Lee, and F. K. McGowan, Phys. Rev. C **53**, 2106 (1996).

[26] G. D. Dracoulis, B. Fabricius, T. Kibédi, A. P. Byrne, and A. E. Stuchbery, Nucl. Phys. **A554**, 439 (1993).

[27] V. P. Janzen, M. P. Carpenter, L. L. Riedinger, W. Schmitz, S. Pilotte, S. Monaro, D. D. Rajnauth, J. K. Johansson, D. G. Popescu, J. C. Waddington, Y. S. Chen, F. Dönau, and P. B. Semmes, Phys. Rev. Lett. **61**, 2073 (1988).

[28] A. J. Kreiner, J. Davidson, M. Davidson, P. Thieberger, and E. K. Warburton, Phys. Rev. C **42**, 878 (1990).

[29] A. J. Kreiner, Nucl. Phys. **A520**, 225c (1990).

[30] A. Bohr and B. R. Mottelson, *Nuclear Structure* (Benjamin, Reading, MA, 1975), Vol. II.

[31] S. T. Belyaev, K. Dan. Vidensk. Selsk. Mat. Fys. Medd. **31**, 1 (1959).

[32] A. B. Migdal, Nucl. Phys. **13**, 655 (1959).

[33] M. P. Carpenter, C. R. Bingham, L. H. Courtney, V. P. Janzen, A. J. Larabee, Z. M. Liu, L. L. Riedinger, W. Schmitz, R. Bengtsson, T. Bengtsson, W. Nazarewicz, J. Y. Zhang, J. K. Johansson, D. G. Popescu, J. C. Waddington, C. Baktash, M. L. Halbert, N. R. Johnson, I. Y. Lee, Y. S. Schutz, J. Nyberg, A. Johnson, R. Wyss, J. Dubuc, G. Kajrys, S. Monaro, S. Pilotte, K. Honkanen, D. G. Sarantites, and D. R. Haenni, Nucl. Phys. **A513**, 125 (1990).

[34] R. A. Bark, G. D. Dracoulis, A. E. Stuchbery, A. P. Byrne, A. M. Baxter, F. Riess, and P. K. Weng, J. Phys. G **15**, L169 (1989).

[35] S. Juutinen, P. Ahonen, J. Hattula, R. Julin, A. Pakkanen, A. Virtanen, J. Simpson, R. Chapman, D. Clarke, F. Khazaie, J. Lisle, and J. N. Mo, Nucl. Phys. **A526**, 346 (1991).

[36] H.-Q. Jin, L. L. Riedinger, C.-H. Yu, W. Nazarewicz, R. Wyss, J.-Y. Zhang, C. Baktash, J. D. Garrett, N. R. Johnson, I. Y. Lee, and F. K. McGowan, Phys. Lett. B **277**, 387 (1992).

[37] W. Nazarewicz, J. Dudek, R. Bengtsson, T. Bengtsson, and I. Ragnarsson, Nucl. Phys. **A435**, 397 (1985).

[38] W. Reviol, H.-Q. Jin, and L. L. Riedinger, Phys. Lett. B **371**, 19 (1996).

[39] F. Rösel, H. M. Fries, K. Alder, and H. C. Pauli, At. Data Nucl. Data Tables **21**, 291 (1978).

[40] G. Hebbinghaus, T. Kutsarova, W. Gast, A. Krämer-Flecken, R. M. Lieder, and W. Urban, Nucl. Phys. **A514**, 225 (1990).

[41] L. Hildingsson, W. Klamra, Th. Lindblad, C. G. Linden, C. A. Kalfas, S. Kossionides, C. T. Papadopoulos, R. Vlastou, J. Gizon, D. Clarke, F. Khazaie, and J. N. Mo, Nucl. Phys. **A513**, 394 (1990).

[42] R. A. Bark, S. W. Ødegård, R. Bengtsson, I. G. Bearden, G. B. Hagemann, B. Herskind, F. Ingebretsen, S. Leoni, H. Ryde, T. Shizuma, K. Strähle, P. O. Tjøm, and J. Wrzesinski, Phys. Rev. C **52**, R450 (1995).

[43] Ts. Venkova, T. Morek, R. M. Lieder, W. Gast, G. Hebbinghaus, A. Kramer-Flecken, W. Urban, G. Sletten, and K. H. Maier, Z. Phys. A **334**, 385 (1989).

[44] A. Neskakis, R. M. Lieder, H. Beuscher, W. F. Davidson, M. Muller-Veggian, and C. Mayer-Boricke, Nucl. Phys. **A261**, 189 (1976).

[45] B. Cederwall, R. Wyss, A. Johnson, J. Nyberg, B. Fant, A. M. Bruce, J. N. Mo, and J. Simpson, Phys. Rev. C **43**, R2031 (1991).

[46] D. L. Balabanski, W. Gast, G. Hebbinghaus, A. Kramer-Flecken, R. M. Lieder, T. Morek, T. Rzaca-Urban, H. Schnare, and W. Urban, Z. Phys. A **332**, 111 (1989).